Binge Feeding Promotes Appetite via Modulating Olfactory Flavor Representation

Hung Lo羅鴻[1,2,†], Malinda L.S. Tantirigama[3,4,‡], Anke Schoenherr[1], Laura Moreno-Velasquez[1], Lukas Faiss[1,5], Benjamin R. Rost[1,5], Matthew E. Larkum[3], Benjamin Judkewitz[1,2,4], Katharina Stumpenhorst[6], Marion Rivalan[4], York Winter[6], Dietmar Schmitz[1,2,4,5,7,8,*], Friedrich W. Johenning[1,2,*,†]

[1]Charité-Universitätsmedizin Berlin, corporate member of Freie Universität Berlin and Humboldt-Universität zu Berlin, Neuroscience Research Center; 10117 Berlin, Germany.

[2]Charité-Universitätsmedizin Berlin, corporate member of Freie Universität Berlin and Humboldt-Universität zu Berlin, Einstein Center for Neurosciences Berlin; 10117 Berlin, Germany.
[3]Humboldt Universität zu Berlin, Institut für Biologie; Charitéplatz 1, Berlin; 10117 Berlin, Germany.

[4]Charité-Universitätsmedizin Berlin, corporate member of Freie Universität Berlin and Humboldt-Universität zu Berlin, NeuroCure Cluster of Excellence; 10117 Berlin, Germany.

[5]German Center for Neurodegenerative Diseases (DZNE) Berlin; 10117 Berlin, Germany.

[6]Humboldt Universität zu Berlin, Cognitive Neurobiology;
Philippstraße 13, Berlin; 10115 Berlin, Germany.

[7]Humboldt Universität zu Berlin, Bernstein Center for Computational Neuroscience;
Philippstraße 13, Berlin; 10115 Berlin, Germany.

[8]Max Delbrück Center for Molecular Medicine in the Helmholtz Association;
Robert-Rössle-Straße 10, 13125 Berlin, Germany

[‡]Present address: Kavli Institute for Systems Neuroscience and Centre for
Neural Computation, Norwegian University of Science and Technology (NTNU);
Trondheim, 7491, Norway.

[*] These authors equally supervised this work. [†] To whom correspondence should be addressed:
E-mail: hung.lo@charite.de, friedrich.johenning@charite.de

Abstract

Binge eating commonly leads to overeating (1; 2; 3; 4), but the exact mechanism is unclear. While it is known that experiencing flavor contributes to satiety, the interactions between flavor, feeding rate, and food intake remain unknown. Here, we demonstrate a novel feeding rate-dependent feedback loop between olfactory flavor representation in the anterior olfactory (piriform) cortex (aPC) and food intake. We developed a liquid food delivery system that allows food consumption at different feeding rates. Using miniscopes for *in vivo* calcium imaging in freely foraging mice, we identified specific excitatory neuronal responses to food and water during slow feeding. Switching to binge feeding transformed these specific responses into unspecific global suppression of neuronal activity. In the gustatory cortex and the olfactory bulb, we observed similarities in flavor representation during binge and slow feeding. Food consumption was predicted by the degree of suppression of neuronal activity in the aPC during binge feeding. Also, food deprivation enhanced neuronal activity suppression. We confirmed the hypothesis that aPC suppression promotes food intake with closed-loop optogenetics experiments. Together, our results show that olfactory sensory representation in the aPC reciprocally interacts with consummatory behavior to enhance food intake.

Keywords: Binge eating, flavor, smell, taste, Ca^{2+} imaging, optogenetics

Introduction

Eating rapidly in a short period, commonly known as binge eating, reduces satiation, the process leading to satiety. Therefore, eating proceeds beyond homeostatic needs (5; 6). Satiation is an important feedback signal that reduces food consumption upon food intake. The soup paradox illustrates the intimate relationship between feeding rate and satiation: Energy-dense liquids, like apple juice, offer less long-term satiety compared to their isocaloric solid counterparts, such as apples. Interestingly, however, when the rate of liquid food intake is slowed down, for example, with spoon feeding, its ability to satisfy hunger matches that of solid foods, influencing 24-hour food intake (7). The canonical explanation for the reduction of satiation by binge feeding in comparison to slow feeding is based on the delayed transfer of homeostatic signals from the gastrointestinal tract to the brain (8; 9; 10). While visceral satiation based on ingestion and absorption is undisputed, there is also sensory satiation mediated by flavor perception (11; 12; 13; 14). However, no study has investigated whether alterations in flavor representation during binge feeding can reduce sensory satiation. Such a feedback loop between feeding behavior, appetite, and flavor representation would support the emerging concept that reciprocal interactions between action and perception shape behavior (15).

Flavor is a multisensory phenomenon involving multiple interconnected primary sensory areas including the primary olfactory cortex or piriform cortex (PC) representing smell, the gustatory cortex (GC) representing taste, and, to some degree, other sensory cortices for tactile and visual aspects of food (16; 17). The PC generally represents odor identity in a concentration-invariant population code of activated neurons (18). Random activation of neuronal subpopulations in the PC can determine conditioned appetitive and aversive behavioral responses (19), and the PC population code does not contribute to the signaling of odor valence (20). If the PC's role in flavor representation during feeding were limited to identification without affecting specific behavioral outcomes, we would expect a stable representation of flavors in the neuronal response patterns to slow and binge feeding.

Results

Feeding rate modulates flavor representation in the anterior piriform cortex

To examine how feeding rate affects sensory representation, we established a feeding paradigm combined with calcium (Ca^{2+}) imaging in freely moving mice. We built a liquid food delivery system that feeds mice at two different rates to experimentally induce slow or binge feeding. Mice could voluntarily lick from a lick spout to trigger the delivery of a droplet ($\sim$1.8 μL) of liquid food (Ensure, artificial energy-dense flavored nutrient solution) or water. Over 30 min, mice had access to the spout for a total of 14 minutes, with a pseudorandom order of 2 min long slow and fast feeding periods. To control the feeding rate, we implemented different refractory periods for the delivery pump: 4 seconds for the slow feeding mode and 0.4 seconds for the binge feeding mode (1a). Mice consumed more food and licked at a higher rate during binge feeding (Fig. S1a-d).

To record feeding-related neuronal activity patterns in the anterior olfactory (piriform) cortex (aPC), we used endomicroscopic lenses (GRIN lenses) attached to prisms combined with a miniscope to image Ca^{2+} transients of excitatory aPC neurons expressing GCaMP6f (Fig. 1b, and Fig. S3a-c). We were able to stably record around 140 aPC excitatory neurons per individual imaging session (Fig. S3d, average = 140.40 ± 72.19 neurons).

When switching from slow feeding to binge feeding, we observed a robust suppression of the aPC excitatory neuron population activity (Fig. 1c, Supplementary Video S1). We categorized neurons based on their responses during slow feeding, as this feeding mode provided a larger number of clearly separated individual trials. We interspersed brief water deliveries in the slow feeding mode to differentiate food-specific neurons from non-specific feeding-related neurons. This protocol allowed us to classify neurons pooled over animals and sessions into food-activated (10.5%), water-activated (13.8%), non-selective consumption-activated (neurons responding to both food and water deliveries; 2.0%), and non-responders (73.7%; Fig. 1d, e and Fig. S2a-b). Binge feeding-induced aPC suppression was present in food-activated, water-activated, and non-responding neurons but not in non-selective consumption-activated neurons (Fig. 1f, g, Fig. S2c-f, statistical analysis of the neuronal activity differences during slow and binge feeding are illustrated with Q-values (unpaired t-test with false discovery rate correction) along the averaged Ca^{2+} traces).

Activity in the PC represents odor identity through a distributed population code and transmits information about odor identity and concentration to downstream targets (21; 22; 23; 24; 25; 26). The percentage of cells in the food-specific subclass during slow feeding is comparable to odor-specific populations observed in the aPC (26; 27). When odors are presented at different intensities, the distributed population code and the neuronal firing rates remain similar (24). So, in spite of the higher food volume over time during binge feeding resulting in increased intensity of flavors of the same identity, we did not expect changes in the population code (Fig. 1g, 2e). Thus, our data points to a feeding rate-dependent modulation of flavor representation in the aPC that fundamentally alters the flavor-specific population code.

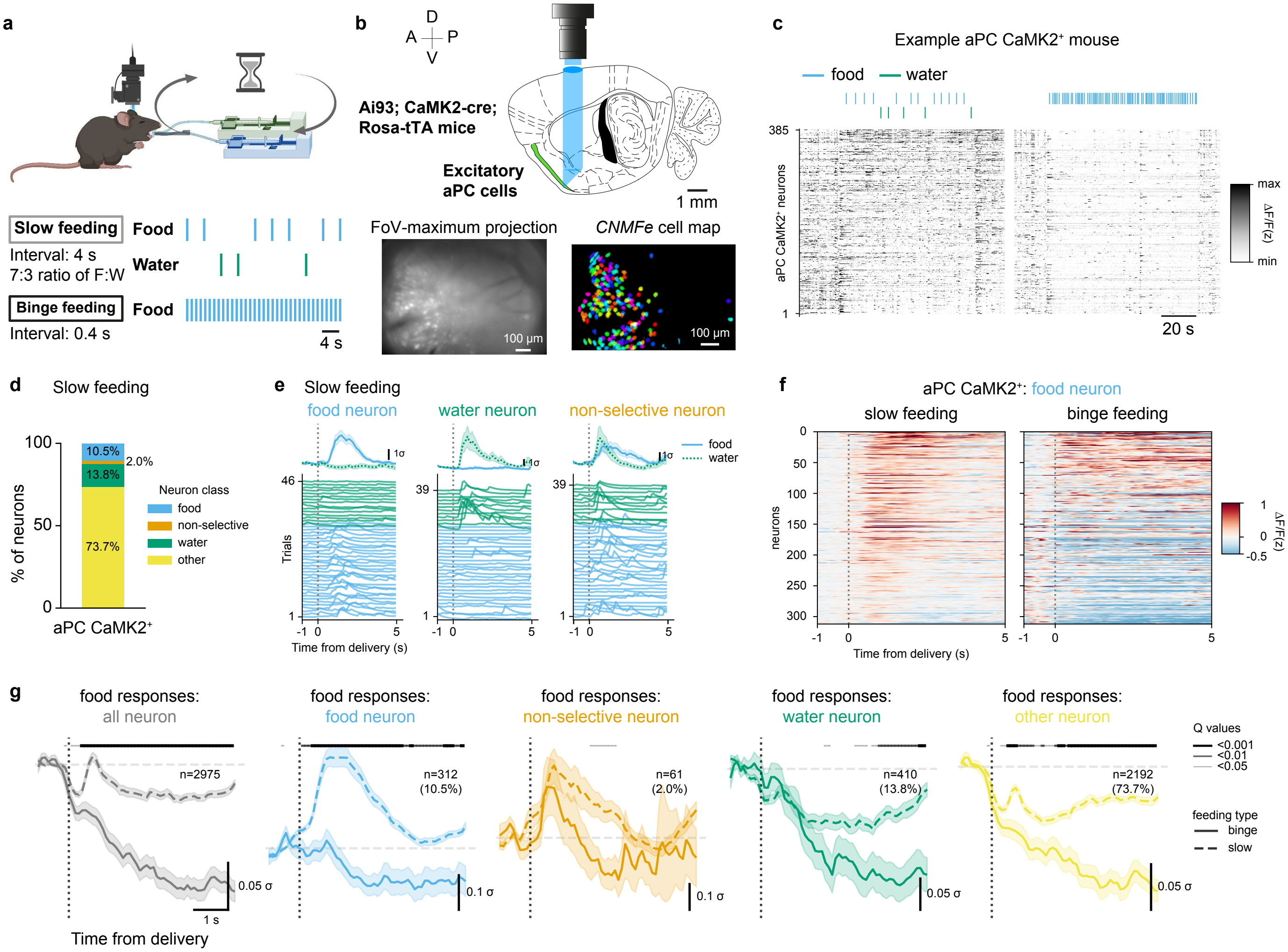

Figure 1: **Feeding rate modulates flavor representations in the aPC.**
a, Miniscope recording and behavioral protocol for slow feeding and binge feeding. **b**, Top: Schematics of GRIN lens/Prism (blue shade) implantation in the aPC (green structure). Bottom: Field-of-view of miniscope recordings and extracted cell maps by constrained non-negative matrix factorization (*CNMFe*). **c**, Example Ca^{2+} traces of aPC neurons during slow feeding and binge feeding from one mouse. **d**, Percentage of aPC neurons activated during slow feeding by food, water, or non-selective consumption vs. non-responding neurons. (n=2975 cells, 481 slow feeding trials, and 241 binge feeding trials in 8 mice). **e**, Trial-average and single trial responses of example aPC food-activated, water-activated, and non-selective neurons upon slow feeding. **f**, Trial-averaged responses to food deliveries of individual aPC $CaMK2^+$ food-activated neurons upon slow feeding and binge feeding (n=312 cells in 8 mice). **g**, Trial-average responses of population and subclasses of aPC $CaMK2^+$ neurons upon slow and binge feeding (n is the same as in **d**). The dashed vertical line indicates the start of the food delivery. The shaded line above denotes the adjusted P-values (Q-values) of each time point, with different line widths representing different values (from thin to thick: Q <0.05, <0.01, <0.001). For **e**, **g**, data are shown as mean ± s.e.m.

Flavor representation in the gustatory cortex is stable across feeding rates

In general in sensory systems, behavior has profound effects on brain activity underlying the representation of sensory inputs (28; 29; 30; 31; 32; 33). Therefore, neuronal suppression in the aPC induced by binge feeding could be a more global phenomenon that might be observed in other brain regions involving flavor representation. To test this, we performed Ca^{2+} imaging in the gustatory cortex (GC, granular, and dysgranular insular cortex) using a miniscope and tracked taste representation during slow and binge feeding (Fig. 2a-c, Fig. S4a-g). We found little modulation in the general population of GC neurons upon binge feeding compared with slow feeding (Fig. 2d), except for prolonged activation of GC neurons during binge feeding (Fig. 2d). in GC water-activated, non-selective and non-responding neurons, binge feeding of food had minimal levels of modulation compared with the general suppression in aPC neurons. (Fig. 2e, Fig. S5a; estimated effect sizes in each neuron class for aPC and GC neurons). Unlike the global activity suppression of the food-activated neurons in the aPC, food-specific activation of GC neurons was selectively preserved during binge feeding (Fig. 2d, e, and Fig. S5b).

To further analyze these distinct modes of flavor representation across the two cortices, we correlated the single-cell activity between binge and slow feeding in food-activated neurons in the aPC and the GC. In the GC, the activation level of food-activated neurons during slow feeding linearly correlates with the activity changes during binge feeding (Fig. 2f). In the aPC, however, we found no correlation between responses during slow and binge feeding, suggesting that binge-induced activity modulation is independent of the neuronal responses during slow feeding (Fig. 2f). The cumulative distribution of the amplitude difference between binge and slow feeding shows that in the GC, the net reduction is smaller and a larger fraction of cells show an increased binge feeding related neuronal response compared to the aPC (Fig. 2g). We interpret our finding as a non-uniform, general inhibition during binge feeding (34). Thus, flavor representation in the GC is preserved during binge feeding, whereas binge feeding induces a generalized activity suppression in the aPC (Fig. 2h).

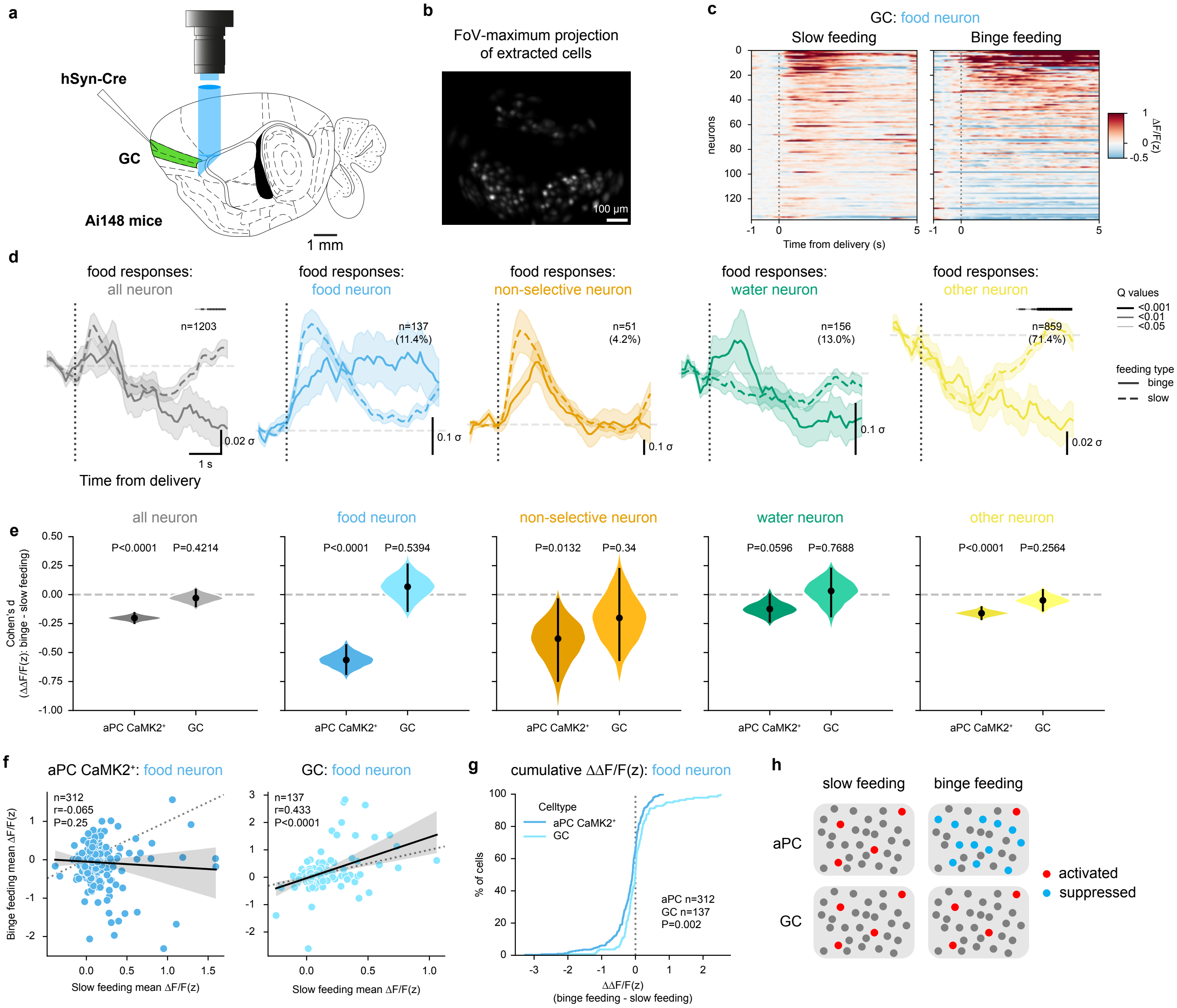

Figure 2: **Flavor representation in the GC is stable across feeding rates.**
a, Schematics of GRIN lens/Prism implantation in the GC. **b**, Cell maps extracted by *CNMFe*. **c**, Trial-averaged responses of individual GC food-activated neurons upon slow feeding and binge feeding (n=137 from 3 mice). **d**, Trial-averaged responses of the whole population and subclasses of GC neurons upon slow and binge feeding (n=1203 cells from 3 mice). The shaded line above denotes the adjusted P-values (Q-values) of each time point, with different line widths representing different values (from thin to thick: Q <0.05, <0.01, <0.001). **e**, Estimated effect size (Cohen's d) of binge feeding-induced modulation in the aPC CaMK2$^+$ and GC neurons within individual subclasses. P-values are calculated with the permutation test with 5000 times bootstrapping (n is the same as in **d**). **f**, Cell-wise comparison of neuronal responses upon slow feeding and binge feeding in food-activated aPC CaMK2$^+$ and GC neurons (n is the same as in Fig. 1**f** and in **c**).

g, Cumulative distribution of the difference (binge feeding vs. slow feeding) of z-scored ΔF/F (ΔΔF/F(z)) in food-activated aPC CaMK2$^+$ and GC neurons (n is the same as in **f**). **h**, Schematics of neuronal responses in the aPC and the GC during slow feeding and binge feeding.

For **d**, data are shown as mean ± s.e.m. For **e**, data are shown as means of bootstrapped effect sizes (Cohen's d) ± 95% confidence interval. For **f**, r and P represent the correlation coefficient and P-value of Pearson's r. For **g**, the P-value is calculated from the Kolmogorov-Smirnov test.

Binge feeding-induced anterior piriform cortex suppression is not inherited from the olfactory bulb

The aPC is the first cortical relay of the olfactory system and receives sensory afferent inputs from the olfactory bulb (35). We tested if a reduction in sensory input from the olfactory bulb could explain global suppression during binge feeding in the aPC. To this end, we performed *in vivo* head-fixed 3-photon Ca^{2+} imaging in the olfactory bulb (OB) mitral cells during binge feeding. Mitral cells are the major neuron population propagating odor information to higher olfactory cortices, including aPC (18), and OB mitral cells remained activated upon binge feeding (Fig. 3a-c, Fig. S6a,b). At the population level, net excitatory OB output to the aPC was similar during slow and binge feeding (Fig. 3d). These findings align with the observation that intracortical connections and not the sensory afferents dominate neuronal activity in the aPC (36). We conclude that binge feeding-induced aPC suppression is not inherited from the OB.

Binge feeding-induced anterior piriform cortex suppression extends to the major classes of local GABAergic neurons

Since the excitatory sensory drive is unaffected by feeding rate, enhanced recruitment of inhibitory interneurons during binge feeding could underlie the global suppression of the aPC. Local inhibitory feedback interneurons – activated by recurrent excitatory activity – predominantly inhibit odor responses in the aPC, whereas the contribution of feedforward interneurons is minor (37). We next probed the activity levels of aPC PV$^+$ and SST+ inhibitory interneurons during slow and binge feeding with miniscope Ca^{2+} imaging, as they cover a large proportion of local feedback circuits (38). Both PV+ and SST+ interneurons show strong suppression upon binge feeding. In contrast, the population responses of both types of interneurons showed net activity increases during slow feeding (Fig. 3e-l, Fig S7a-f, Fig S8a-c). Therefore, changes in the excitation-to-inhibition ratio of sensory afferent and local recurrent aPC circuits do not seem to mediate the global suppression of aPC activity during binge feeding. The binge feeding-induced suppression of activity in the aPC affects both the excitatory neurons and the major classes of local inhibitory interneurons. Therefore, binge feeding-induced suppression globally affects most local circuits in the aPC.

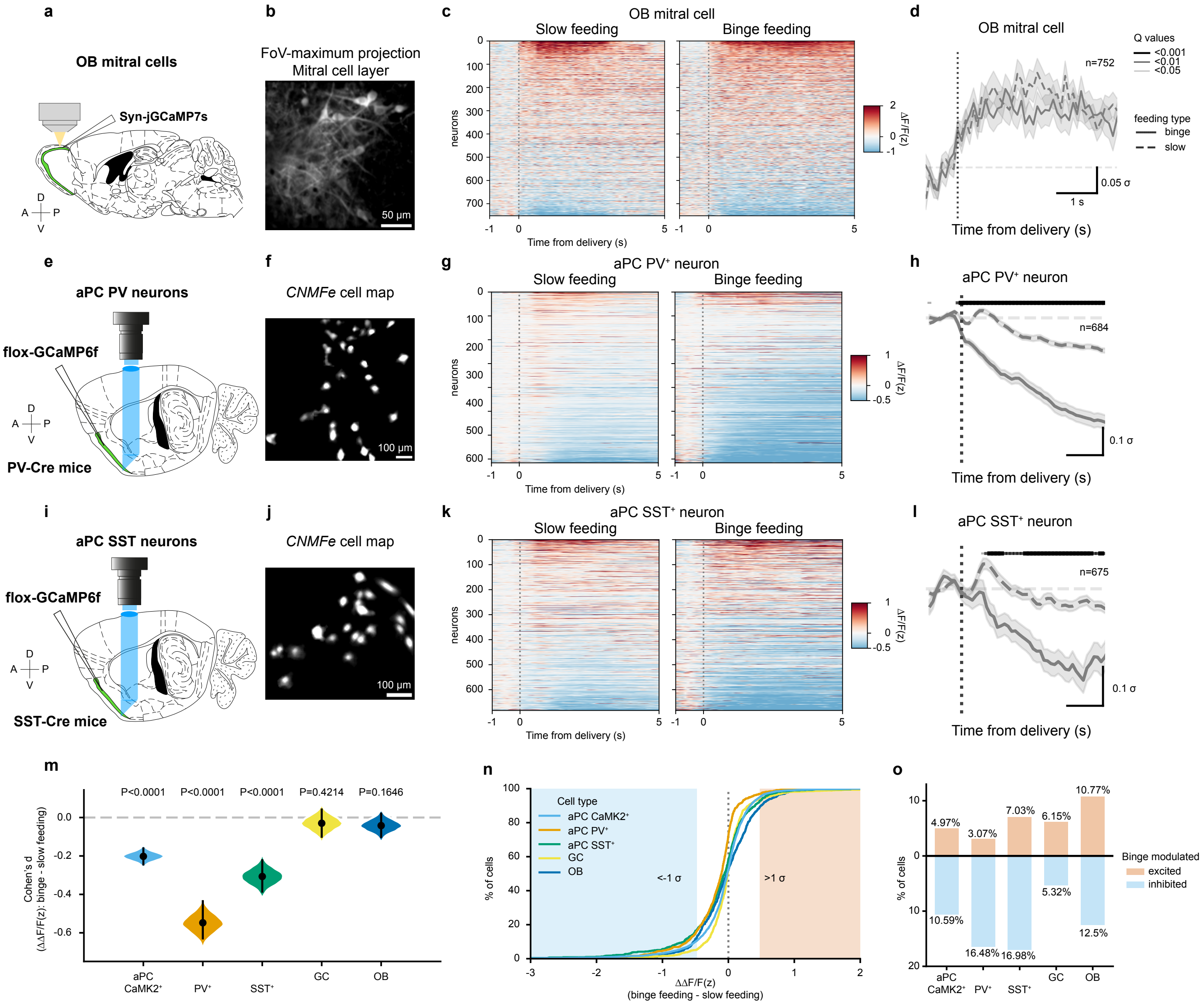

Figure 3: **Binge feeding-induced aPC suppression is not inherited from the OB and extends to GABAergic aPC neurons.**

a, Schematics of 3P-Ca^{2+} imaging in OB mitral cells. **b**, FoV of OB mitral cells. **c**, Trial-average of individual OB mitral cells upon slow and binge feeding (n=752 cells from 4 mice). **d**, Trial-average of OB mitral cell population responses upon slow and binge feeding (n is the same as in **c**). **e**, Schematics of Ca^{2+} imaging in aPC PV^{+} neurons. **f**, Cell map of aPC PV^{+}neurons extracted by *CNMFe*. **g**, Trial-average of individual aPC PV^{+}neurons upon slow and binge feeding (n=684 cells from 3 mice). **h**, Trial-average of population aPC PV^{+}neuron responses upon slow and binge feeding (n is the same as in **g**). **i**, Schematics of Ca^{2+} imaging in aPC SST^{+}neurons. **j**, Cell map of aPC SST^{+} neurons extracted by *CNMFe*. **k**, Trial-average of individual aPC SST^{+} neurons upon slow and binge feeding (n=675 cells from 3 mice).

l, Trial-averaged of population aPC SST$^+$ neuron responses upon slow and binge feeding (n is the same as in **k**). **m**, Estimated effect sizes of binge-induced modulation in aPC CaMK2$^+$, aPC PV$^+$, aPC SST$^+$, GC, and OB mitral cells. **n**, Cumulative distribution of binge-induced modulation of ΔF/F(z) in aPC CaMK2$^+$, aPC PV$^+$, aPC SST$^+$, GC, and OB mitral cells. **o**, Percentages of binge feeding modulated population in aPC CaMK2$^+$, aPC PV$^+$, aPC SST$^+$, GC, and OB mitral cells.

For **d**, **h**, **l**, data are shown as mean ± s.e.m, and the shaded line above denotes the adjusted P-values (Q-values) of each time point, with different line widths representing different values (from thin to thick: $Q < 0.05$, < 0.01, < 0.001). For m, data are shown as means of bootstrapped effect sizes (Cohen's d) ± 95% confidence interval.

Magnitude of binge feeding-induced anterior piriform cortex suppression correlates with appetite and depends on olfactory perception and metabolic state

Flavor perception of food items contributes to satiation and bypassing flavor perception via an intragastric catheter reduces satiation and accelerates gastric emptying of identical food items (13). The suppression of neuronal activity, specifically in the aPC described here, reduces the sensory representation of food items. Accordingly, we hypothesized that the aPC suppression during binge feeding could constitute a mechanistic link between a sensory neuronal response pattern in the flavor system and decreased satiation. Under *ad libitum* feeding conditions, mice consumed different amounts of food on different experimental days, which we take as a proxy for differences in satiation. This noticeable behavioral variability in our recording sessions correlates with temporal progression, suggesting binge feeding gradually escalates over time (Fig S9a). We, therefore, investigated whether this behavioral variability maps onto the aPC neuronal responses. Using a linear mixed model, we found a robust time-independent correlation between the initial binge eating-induced aPC suppression and subsequent food consumption on each recording session ((Fig. 4) b). Suppression was always quantified during the onset of a binge bout within the first 4 seconds after initiation. Our model, therefore, quantifies suppression independently of feeding duration. The strong correlation between neuronal activity patterns and food intake does not exist for slow feeding aPC responses ((Fig. 4) b,c). We also observed consumption-correlated suppression of neuronal activity in aPC PV$^+$ neurons. In contrast, aPC SST$^+$+ neurons and GC neurons did not show a correlation between neuronal activity and food intake. (Fig. S9c). These findings suggest that consumption-correlated neuronal modulations are mostly restricted to the olfaction component of flavor perception.

We further examined the necessary factors for the consumption-correlated generalized suppression of aPC neuronal activity during binge feeding. To test whether the olfactory perception of the food items is a necessary for consumption-correlated suppression of neuronal activity, we performed nasal lavage with 0.5% Triton solution to induce temporary anosmia in mice (39) ((Fig. 4) d,e anosmia verified by buried food test). We performed imaging experiments before and after the intervention. Our procedure caused a 30% drop on average in the number of active neurons in the field of view detected with imaging, consistent with reduced olfactory inputs to the aPC (Fig. S9b). We then compared the correlation of the aPC activity suppression to consumption in the same mice before and after the anosmia-inducing treatment. In contrast to the pre-anosmia condition, anosmia-inducing treatment abolishes the correlation between the suppression of aPC neuronal activity and consumption ((Fig. 4) f,g). Under anosmia, we still observed binge eating-induced aPC suppression ((Fig. 4) h) in the presence of generally enhanced food intake ((Fig. 4) f). This result suggests that intact sensory olfactory perception is a prerequisite for binge eating-induced aPC suppression correlated to consumption. Metabolic states like hunger and satiety profoundly affect sensory systems (40; 41; 42; 43; 44). Consequently, we wondered if changes in the metabolic state affect the consumption-correlated suppression of aPC neuronal activity during binge feeding. We altered the metabolic state of mice by overnight fasting. We found enhanced food intake in these mice and enhanced binge feeding-induced suppression of aPC neuronal activity compared to *ad libitum*-fed conditions ((Fig. 4) i-l). Under fasting, the correlation between food consumption and aPC neuronal activity suppression is lost ((Fig. 4) j). An increase in suppression was also observed in the GC of fasted mice ((Fig. 4) k,l). We conclude that the suppression of neuronal activity during binge feeding in the aPC is enhanced by fasting and is also observed in the GC.

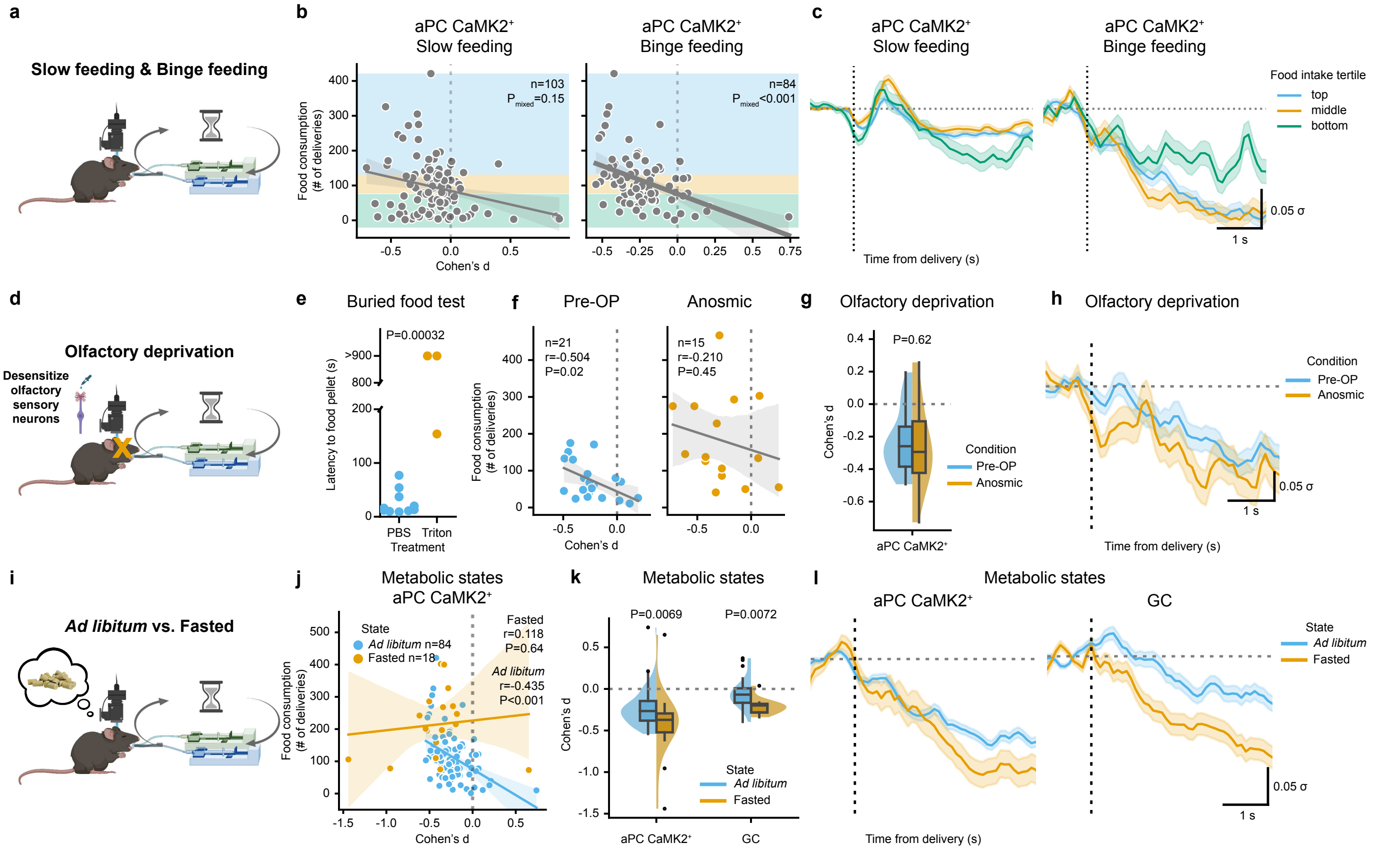

Figure 4: **Magnitude of binge feeding-induced anterior piriform cortex suppression correlates with appetite and depends on olfactory perception and metabolic state.**
a, Schematics of feeding and Ca^{2+} imaging paradigm. **b**, Correlations between session-specific food intake and modulation of neuronal activity in aPC CaMK2^{+} neurons upon slow and binge feeding (n=103 slow feeding sessions and 84 binge feeding sessions from 8 mice). **c**, Trial-average responses of aPC CaMK2^{+} neurons upon slow and binge feeding clustered by food intake (n=34, 35, 34 sessions for top, middle, bottom clusters in slow feeding from 8 mice, n=28, 28, 28 sessions for top, middle, bottom clusters in binge feeding from 8 mice). **d**, Schematics of anosmic paradigm. **e**, Latency of mice finding the buried food pellet 48 hrs after treatment (n=10 mice for PBS treated group, n=3 for Triton treated group). **f**, Correlations between session-specific food intake and modulation of neuronal activity in aPC CaMK2^{+} neurons upon binge feeding with intact olfaction and under anosmic conditions (n=21 Pre-OP sessions and n=15 Anosmic sessions from the same 3 mice). **g**, Binge-induced modulation of neuronal activity with intact olfaction and under anosmic conditions (n is the same as in **f**). **h**, Trial-averaged activity of aPC CaMK2^{+} neurons upon binge feeding with intact olfaction and under anosmic conditions (n is the same as in **f**). **i**, Schematics of fasting paradigm. **j**, Correlations between session-specific food intake and modulation of neuronal activity in aPC CaMK2^{+} neurons upon binge feeding under *ad libitum* or overnight fasted conditions (n=18 fasted sessions from 5 mice, n for *ad libitum* conditions is the same as in **b**). **k**, Binge-induced modulation of neuronal activity under *ad libitum* or overnight fasted conditions (n is the same as in **j**).

l, Trial-averaged responses of aPC CaMK2^{+} neurons upon binge feeding under *ad libitum* or overnight fasted conditions (n is the same as in **j**).

For **c**, **h**, **l**, data are shown as mean ± s.e.m. For **f**, **j**, r and P represent the correlation coefficient and P-value of Pearson's r. For **b**, P represents the significance level of Cohen's d to food consumption by a linear mixed model. For the box plot in g and k, the center line shows the median, the box limits show the quartiles, the whiskers show 1.5x the interquartile range, and the points show the outliers.

Optogenetically suppressing anterior piriform cortex neurons promotes feeding

We have so far established the correlative relationship between feeding rate, olfactory flavor representation, and metabolic state. While binge feeding and appetite clearly covary with global activity suppression in the aPC, it is unclear if the sensory effect we observe is an epiphenomenon (***H0***, Fig. 5a) or reciprocally interacts with feeding behavior in a feedback loop (***H1***, Fig. 5a). We, therefore, next asked whether there was a causal relationship between suppressed aPC activity and feeding behavior by inhibiting aPC during feeding. This tested if aPC suppression alone is sufficient to increase food consumption (***H1***, Fig. 5a). We employed a closed-loop optogenetic inhibition paradigm to silence aPC excitatory neurons at the initiation of binge feeding bouts (Fig. 5b,e). To suppress activity at the behavioral timescale (tens of seconds) of binge feeding bouts while minimizing the illumination period, we chose the highly light-sensitive mosquito opsin eOPN3 (45) to provide long-lasting suppression of recurrent excitatory fibers in the aPC (Fig. S10c for optical fiber implant coordination). We found that mice consumed more food when aPC activity was optogenetically suppressed upon feeding (Fig. 5f-i). The optogenetic suppression of aPC activity prolonged the individual feeding bouts, while the number of feeding bouts remained similar, suggesting that optogenetic aPC suppression predominantly affects consummatory and not appetitive behavior (Fig. 5f and Fig. S10a,b). Light stimulation alone did not affect feeding behaviors in control mice transduced with AAVs encoding tdTomato (Fig. 5g-i). Our data infers that binge feeding-induced aPC suppression is causally linked to feeding behaviors, suggesting a functional role of binge feeding-induced aPC suppression in modulating appetite (***H1***, Fig. 5a)

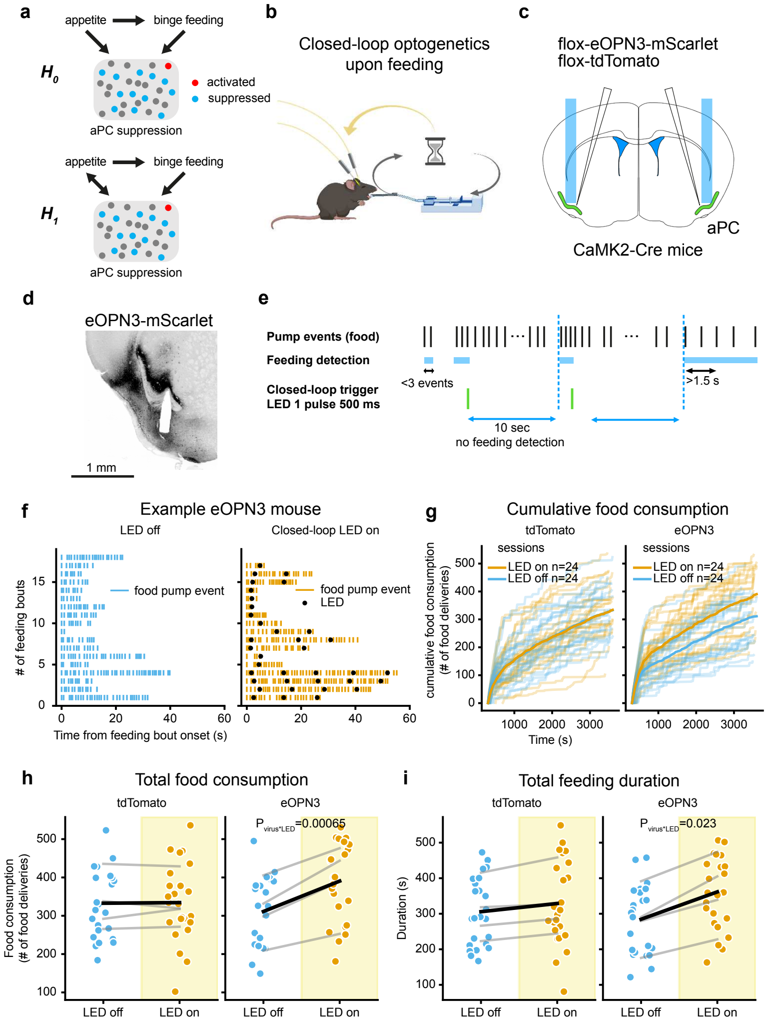

Figure 5: **Optogenetically suppressing aPC neurons promotes feeding.**
a, Schematics of hypotheses on relationships of appetite, binge feeding and aPC suppression. **b**, Schematics of closed-loop optogenetics experiment setup and feeding paradigm. **c**, Schematics of viral injection and optical fiber implants bilaterally in the aPC. **d**, Brain slice with optical fiber implant path. **e**, Schematics of feeding-based closed-loop optogenetics paradigm. **f**, Example feeding bouts in an eOPN3-expressing mouse without light stimulation (left panel) and with closed-loop light stimulation (right panel). **g**, Cumulative feeding events through experimental sessions for mice expressing tdTomato (left panel, n=12 LED off and 12 LED on sessions from 4 mice) and mice expressing eOPN3 (right panel, n=12 LED off and 12 LED on sessions from 4 mice). **h**, Effects of light stimulation on total food consumption in tdTomato- and eOPN3-expressing mice (n is the same as in **g**). **i**, Effects of light stimulation on total feeding duration in tdTomato- and eOPN3-expressing mice (n is the same as in **g**). For **h**, **i**, grey lines denote the data from the same mice, and the black line denotes the mean. The P-values are calculated from a linear mixed model (see **Methods**).

Discussion

The role of olfactory flavor representation during feeding behaviors is poorly understood despite its essential contribution to flavor experience (46; 47). Using cell-type specific *in vivo* Ca^{2+} imaging and optogenetics in freely behaving mice, we provide circuit-level evidence that suppression of flavor representation in the aPC during binge feeding actively enhances food intake. While chronic effects of olfactory alterations on food intake and metabolism have been reported (48; 49), we found an acute functional role of olfaction at the level of individual feeding bouts. Our findings suggest that the olfactory representation of flavor during feeding provides feedback for sensory satiation to modulate food intake and homeostasis in real-time.

Metabolic states have profound effects on sensory systems, especially olfaction. Hunger increases neuronal and behavioral responses to odors, and in contrast, satiety decreases them (40; 41; 42; 43; 44). Sensory detection of food items leads to a rapid switch in activity patterns from consumption-promoting AgRP neurons to consumption-inhibiting POMC neurons in the arcuate nucleus of the hypothalamus. The amplitudes of these foraging-related switches in hypothalamic activity are enhanced by fasting and sensory signals from food items with a high hedonic value (11; 14; 12). We demonstrated that the amplitude of binge feeding-induced suppression in the aPC reflects internal appetite levels and is enhanced by fasting, supporting that metabolic states strongly modulate olfactory representation during feeding.

The sensory experience of food items contributes to satiety. Bypassing sensory experiences of food within the oral cavity by direct gastric infusion reduces satiety and accelerates gastric emptying compared to regular feeding in humans and rodents (50; 13; 51). Our study supports the idea that suppressed olfactory flavor representation, via direct binge feeding or artificially suppressing the aPC, constitutes an acute intrinsic behavior-associated cortical mechanism leading to more consumption, inferring lower satiety levels. The reciprocity between feeding behavior and olfactory representation demonstrated here (Fig. 5a) extends the emerging theory that perception and action reciprocally interact (15).

From an evolutionary perspective of food scarcity, overeating induced by suppression of sensory satiety would be pro-survival. In the surplus of food environment human beings are facing today, an increased eating rate is commonly linked to overeating (52) and obesity (53), while reducing the eating rate can effectively mitigate food consumption (5; 1; 6). Here, we provide evidence that feeding rate-dependent modulation of olfactory flavor representation modulates appetite (Fig. S11). Our findings add the perspective of sensory experience and awareness to the notion that it is not only what you eat but also how you eat.

Acknowledgements

We thank Susanne Rieckmann, Monika Dopatka, Anny Kretschmer, Katja Czieselsky and Celina Ernst for their excellent technical assistance; Daniel Parthier for his inputs on statistical analysis; Yen-Chung Chen for his inputs on programming; Melissa Long from the Charité Animal Behavioral Phenotyping Facility, Charité Advanced Medical BIOimaging Core Facility, and Charité Viral Core Facility for their assistance; James Poulet and David Owald for their feedback on the manuscript; Robin Blazing and Kevin Franks for sharing *in vivo* optical fiber implantation protocols; Andreas Klaus for his input at the early stage of this study.

Funding

HL is supported by the PhD Fellowship from the Einstein Center for Neurosciences Berlin and the Taiwanese Government Scholarship to Study Abroad.

FWJ is supported by the Deutsche Forschungsgemeinschaft (DFG) (project 458236353 and project 520223756 - SPP2411 LOOPs)

BRR is supported by the DFG (project 327654276 - SFB1315 and project 273915538 - SPP1926).

DS is supported by the DFG (project 184695641 – SFB 958, project 327654276 – SFB 1315, project 415914819 – FOR 3004, project 431572356, the German Excellence Strategy EXC-2049-390688087, NeuroCure), by the European Research Council (ERC) under the European Union's Horizon 2020 research and innovation program (BrainPlay Grant agreement No. 810580) and by the Federal Ministry of Education and Research (BMBF, SmartAge – project 01GQ1420B).

Competing Interest Statement

YW owns PhenoSys equity. Other authors have declared no competing interest.

Author contributions

Conceptualization: HL, DS, FWJ

Methodology: AS, FWJ, KS, MR, YW, MLST, BJ, MEL

Validation: AS, HL, LF, LMV, BRR, FWJ

Formal analysis: HL, FWJ

Investigation: HL, FWJ, MLST, LF, LMV

Resources: MEL, BJ, MR, YW, DS, BRR

Data Curation: HL, FWJ

Writing - Original Draft: HL, FWJ

Writing - Review & Editing: DS, BRR, MR, BJ, KS, MLST, MEL, LF, LMV, YW

Visualization: HL

Supervision: FWJ, DS, MEL, BRR

Project administration: AS, FWJ, DS

Funding acquisition: FWJ, DS

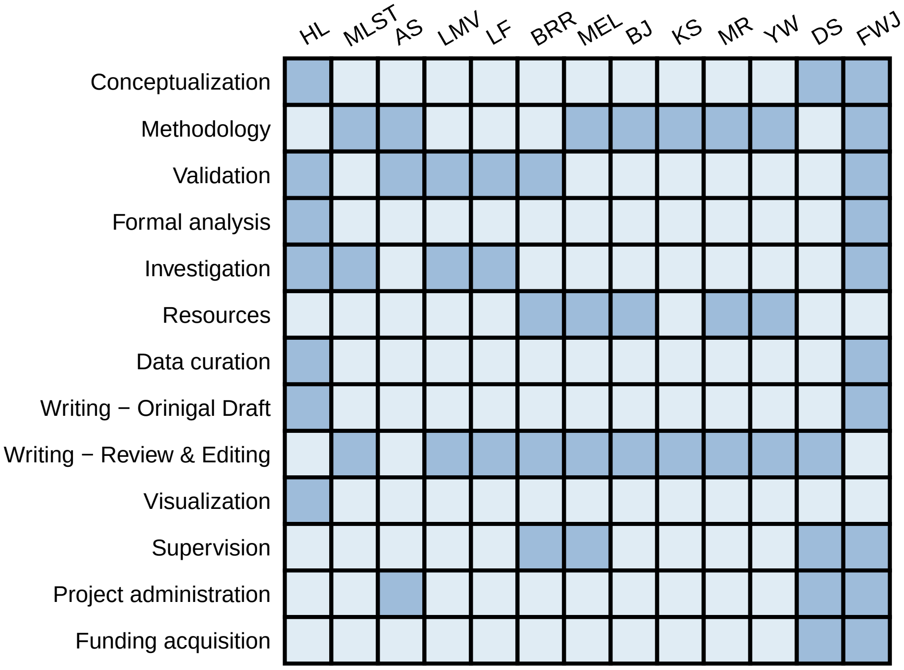

	HL	MLST	AS	LMV	LF	BRR	MEL	BJ	KS	MR	YW	DS	FWJ
Conceptualization	■	□	□	□	□	□	□	□	□	□	□	■	■
Methodology	□	■	■	□	□	□	■	■	■	■	■	□	■
Validation	■	□	■	■	■	■	□	□	□	□	□	□	■
Formal analysis	■	□	□	□	□	□	□	□	□	□	□	□	■
Investigation	■	■	□	■	■	□	□	□	□	□	□	□	■
Resources	□	□	□	□	□	■	■	■	□	■	■	□	□
Data curation	■	□	□	□	□	□	□	□	□	□	□	□	■
Writing − Orinigal Draft	■	□	□	□	□	□	□	□	□	□	□	□	■
Writing − Review & Editing	□	■	□	■	■	■	■	■	■	■	■	■	□
Visualization	■	□	□	□	□	□	□	□	□	□	□	□	□
Supervision	□	□	□	□	□	■	■	□	□	□	□	■	■
Project administration	□	□	■	□	□	□	□	□	□	□	□	■	■
Funding acquisition	□	□	□	□	□	□	□	□	□	□	□	■	■

Author contribution

Data and code availability

Source data for individual figure panel can be found on a GitHub repository (https://github.com/hung-lo/BingeFeeding_2023). Processed data will be deposited to a data repository (figshare or Zenodo) upon acceptance of this manuscript. Raw data will be available upon request due to the large file size (∼2-3 TB). Code for plotting individual figure panel can be found on a GitHub repository (https://github.com/hung-lo/BingeFeeding_2023). All code for data processing and analysis will be deposited to a GitHub repository upon acceptance of this manuscript.

Materials and Methods

Animals

Animals were kept at the animal facility of Charité, under a regular 12/12 hour light-dark cycle. All procedures involving animal experiments were approved by the local authorities and ethics committee (LaGeSo Berlin, license numbers G0278/16, G0313/16, and G0156/20). To image excitatory neurons in the aPC, we cross-bred Ai93D mice, Rosa-tTA mice, and CaMK2-Cre mice to obtain Ai93D; Rosa-tTA; CaMK2-Cre mice that express GCaMP6f in excitatory cells. To prevent early expression of GCaMP during development, the breeding pairs and offspring were fed with Doxycycline-containing food to suppress the expression of GCaMP6f until weaning. Due to suboptimal GCaMP6f expression in the GC in the abovementioned transgenic mice, we injected the AAV virus carrying hSyn-Cre in the GC of Ai148D mice to express GCaMP6f in the GC. To image OB mitral cells, we inject Syn-jGCaMP7s AAV virus in C57BL/6 mice. To image GABAergic neurons in the aPC, we performed viral injection of Cre-dependent GCaMP6f in PV-Cre or SST-Cre mice. For optogenetic experiments, CaMK2-Cre mice were bilaterally injected with Cre-dependent eOPN3 virus or a Cre-dependent tdTomato expressing virus for controls. All experiments including Ca^{2+} imaging and optogenetics are performed between 9 a.m. to 6 p.m. under regular light.

Liquid food delivery system

To reduce stress, we performed experiments inside the animals' home cages. Cages were modified so that we could protrude the motorized lick spout (PhenoSys, Berlin, Germany) into the cage. After a 5-minute baseline period, motorized lick spouts were presented in the cage and primed for liquid delivery for 2 min with 1 min intervals between presentations. During these intervals, the spouts were retracted. For olfactory isolation, we presented the lick spout inside a glass tube with an opening for animals to reach the spout. Air suction from the glass tube limited olfactory responses to the food odor to the time period just before and while mice interacted with the lick spout. Lick spouts were equipped with piezo sensors to register each licking. Licks triggered a 400-ms activation of electrical pumps, which resulted in the delivery of one droplet ($\sim$1.8 μL) of strawberry or chocolate-flavored Ensure (Abbott Laboratories) or water. After delivery, we set a refractory delay period of 4 sec (slow feeding) or 400 ms (binge feeding). During slow feeding, we provided Ensure and water at a ratio of 7 to 3. Four slow-feeding rounds and three binge-feeding rounds were interchanged in a pseudorandom order. Mice were *ad libitum* fed before the experiments, with a maximal period of up to 4 hours of pre-experiment food deprivation during the light cycle. Fasting was performed once a week for 20-22 hours before starting the experiment.

Surgery procedures

Stereotactic injection

Mice were anesthetized by inhalation anesthesia with isoflurane (induction: 4-5%, then 1-2% with oxygen, flow rate 0.5-1 l/min). Mice were local anesthetized with Lidocaine (1-2%) subcutaneous injection preincision. A craniotomy was performed over the stereotactically determined target regions (Table. 1) using a semi-automatic neurostar stereotactic apparatus (Neurostar, Tübingen, Germany). The virus (0.4 to 1 μL) was injected using a 10 μL-Hamilton syringe. Postoperative pain was prevented by Carprofen (5 mg/kg) subcutaneous injection right before surgery and in the first 3 days after surgery. After the surgery, the animals recovered for at least two weeks. In some experiments, implantation of the prism or the optic stimulation fiber was performed right after viral injection.

GRIN lens implantation

Mice (>P50) were anesthetized for the procedure by inhalation anesthesia with isoflurane (induction: 4-5%, then 1-2% with oxygen, flow rate 0.5-1 L/min). Mice were local anesthetized with Lidocaine (1-2%) subcutaneous injection preincision. The anesthetized animals were fixed in the stereotact (Neurostar, Tübingen), and a craniotomy was performed over the stereotactically determined target region (Table. 1). The side length of the quadratic craniotomy was slightly larger than the side length of the prism base, approximately 1.2 mm.The insertion tract was paved by aspiration of brain tissue until $\sim$1 mm above the image plane of the microscope. Aspiration was performed through a thin needle (23G, sharp end) linked to a vacuum pump, the procedure was performed twice to ensure sufficient aspiration of brain tissues. Any small hemorrhagic foci that occurred were staunched by Gelfoam. After removal of the Gelfoam and any pending blood clots, insertion of the microendoscopic lens (GRIN lens attached with a Prism (1 mm diameter, ∼9.1 or ∼4.3 mm long, Inscopix) to the desired image plane is performed at a rate of 100 μm/min according to the coordinates in Table 1. With the aid of an adhesive (VetBond, 3M or TRUGLUE, TRUSETAL) and dental cement (Super-Bond C&B, SUNMEDICAL), microendoscopes with attached baseplates (Inscopix) were fixed to the skull, and the optical surface was protected from contamination by a plastic cap (Inscopix baseplate cover). Postoperative pain was prevented by Carprofen (5 mg/kg) subcutaneous injection right before surgery and in the first 3 days after surgery. In a subset of mice, we did not use microendoscopes with attached baseplates. In this case, the slightly protruding microendoscope was fixed to the skull with adhesive and dental cement, and the optical surface was protected from contamination using a silicone cap. In these mice, a baseplate was fixed in the desired optical plane above the protruding lens in a surgery that was performed at a minimum of four weeks after the lens implant.

Table 1: Coordinates for viral injection and GRIN lens and prism implantation

Brain regions	Coordinates (AP/ML/DV, mm)	Notes
aPC	0.32/-3.5/5.5 0.32/-3.0/5.5	For viral injection For implantation we used the bottom right corner of the prism of GRIN lens
GC	0.26/-3.6/4.0 0.26/-3.0/4.1	For viral injection For implantation we used the bottom right corner of the prism of GRIN lens
OB	4.3-4.6/±0.6 /0.3	For viral injection

Cranial window for olfactory bulb imaging

Mice (C57BL/6, <P40) were anesthetized with isoflurane (induction: 4-5%, then 1-2% with oxygen, flow rate 0.5-1 l/min). Mice were local anesthetized with Lidocaine (1-2%) subcutaneous injection preincision. After the scalp and periosteum were removed, a 3mm craniotomy was made over the two bulb hemispheres. An injection micropipette (tip diameter, 10–20 μm)

was filled with AAV1.Syn.jGCaMP7s.WPRE virus solution (Penn Vector Core), and 100 nl was injected 50 nl/min at a depth of 300 μm in either bulb hemisphere (see Table 1 for coordinates). After injection, a semi-circular <3 mm stack of two glass coverslips, glued to each other using optical adhesive, was fitted into the craniotomy and sealed with cyanoacrylate glue and dental cement. Finally, a light-weight head-post was fixed on the skull over the left hemisphere with light-curing adhesives (RelyX, 3M) and dental cement (Ortho-Jet, Lang Dental). Postoperative pain was prevented by Buprenorphine (0.05-0.1 mg/kg) and Carprofen (5 mg/kg) subcutaneous injection right before surgery and then Carprofen (5 mg/kg) in the first days after surgery. Head-fixed 3-photon imaging experiments began 3 weeks after the virus injection.

Ca^{2+} imaging

Habituation

For freely-moving recordings, before starting the combined behavioral and imaging sessions using Ensure and water, mice were habituated to the lick spout delivery with 10% sucrose solution. Mice had to reach a criterion of 25 sucrose deliveries in slow feeding mode in a 45-minute habituation session before the actual measurements began. Mice were further habituated with additional air suction around the lick spout and dummy scope mounting once they had learned to drink from the lick spout. The habituation period usually lasted ~3 weeks.

For head-fixed recordings, the habituation of mice to head-fixation began at least 5 days prior to imaging. On the first day, the animal was head-fixed on a running wheel for 5 min and then gradually increased each day until it was calm for 1 hour. At least one day before imaging, a lick spout with milk/water within easy reach for licking was introduced.

in vivo imaging: miniscope

The miniaturized microscope (nVista miniscope, Inscopix, CA, USA) was mounted right before the imaging session started without anesthesia. Before the recording started, mice were allowed to explore the home cage for 3-5 minutes. After a baseline period of 5 min, the lick spout protruded according to the protocol described above. For each mouse, the imaging settings

(LED intensity, gain, focus… etc.) were individually tuned to reach a similar level of brightness (mean values around 50-60 A.U. in fluorescence histogram function in Inscopix acquisition software). We recorded at 20 Hz with a single focal plane. Most imaging sessions were 4x spatially down-sampled during acquisition to save storage space. The behavioral system was linked with the Inscopix system using TTL pulses upon pump activation. We performed up to 25 imaging sessions per mouse across 5 weeks, and overnight food deprivation was performed once per week.

in vivo imaging: 3-Photon

Imaging from head-fixed mice was performed with a home-built 3-photon microscope. The laser (Opera-F, pumped by Monaco, Coherent) provided light pulses at 1300 nm wavelength and 1 MHz repetition rate for excitation of jGCaMP7s. The laser output passed a four-pass prism pulse compressor for dispersion compensation. Laser power was adjusted using a motorized half-wave plate and a polarizing beam splitter, and was below 20 mW under the objective. We used a Nikon25x/1.1 objective and dual linear galvanometers at a frame rate of $\sim$10Hz. Image acquisition was synchronized with laser pulses and was controlled by LSMAQ. Time-series images (200 x 200 pixels) were recorded at depths of 200-300 μm below pia at the mitral cell layer.

Triton X-100 application

Nasal lavage with 0.5% of Triton X-100 (in 0.1M PBS) can introduce temporal anosmia in mice for up to 3 weeks (39). Mice were anesthetized with Ketamin (100 mg/Kg), Xylazine (20 mg/Kg) and Acepromazine (3 mg/Kg) intraperitoneal injection. They received Caprofen (5mg/ Kg) subcutaneous injection before and the day after the Triton X-100 (experimental group) or PBS (control group) applications. We applied 40 μL 0.5% Triton X-100 solution to each nostril with a gel loading pipette tip that was advanced for 2-3mm into the nostril. Triton solution was slowly applied with a micropump (Narishige, Japan) over several minutes on each side, with an interval of 5 min between the two nostrils. Foam building up at the opening of the nostrils was an indicator of a successful procedure. Throughout the procedure and until waking up from anesthesia, mice were kept on an inclined plane so that their nostrils were below their trachea and lungs in a heated chamber.

Buried food test

To test the efficacy of Triton-induced anosmia, we examined mice's ability to find a hidden food pellet located 1 cm deep in the bedding of the experimental cage. Mice were overnight food-deprived and habituated to the experimental cage for at least 5 minutes before the experiment started. After the food pellet was buried, mice were transferred into the experimental cage. The time to find the pellet was documented by the experimenter. If the mice did not find the pellet after 15 minutes, the experiment was stopped. Control experiments were performed with mice that had undergone the same lavage procedure with 0.1M PBS nasal lavage. The buried food tests were repeated every week to monitor mice's smell ability to ensure mice remained anosmic throughout our experiments.

Optogenetic experiments

Mice expressing eOPN3 in aPC excitatory neurons were anesthetized for the procedure by inhalation anesthesia with isoflurane (induction: 4-5%, then 1-2% with oxygen, flow rate 0.5-1 L/min). The anesthetized animals were fixed in the stereotact (Neurostar, Tübingen), and a craniotomy was performed over the stereotactically determined target region. Fiberoptic cannulas (200 μm diameter, NA 0.66, length 5mm, Doric lenses) were inserted bilaterally until reaching the target coordinates (Fig. S10c). The slightly protruding fiber with an attached zirconia sleeve for taking up the stimulation fiber patchcord was fixed to the skull with adhesive and dental cement, and the optical surface was protected from contamination using a plastic cap. Before starting the combined behavioral and optogenetic stimulation sessions using Ensure, the mice were habituated to the lick spout delivery with 10% sucrose solution. Mice had to reach a criterion of 25 sucrose deliveries in binge feeding mode and needed to successfully trigger sham closed-loop stimulations in a 20-minute habituation session before the actual measurements began. At the start of the experiment, we plugged a splitter branching patchcord (200 μm diameter, NA 0.57, Doric) connected to a mono fiberoptic patchcord (480 μm diameter, NA 0.63, Doric) onto the fiberoptic cannulas. Light from a Ce:YAG fiber light source (Doric) was delivered at an intensity of 8mW at the tip of the fibers. For these experiments, mice were granted constant access to the lick spout in the binge feeding mode over a period of 60 min. Upon detection of a binge bout (3 pump deliveries with a maximum of a 1.5 s interdelivery interval), a 500 ms light stimulus was delivered on "LED on" days. After the detection of a binge bout with a subsequent light stimulus, there was a minimal refractory period of 10 seconds until a binge bout could initiate the next light stimulus. Everything was similar on "LED off" days, apart from not stimulating with light upon binge bout detection. LED on and off days were alternated for 12 subsequent days.

Imaging processing

Ca^{2+} movies obtained from miniscope recordings were first temporally downsampled to 10 Hz. We then cropped out regions in the field of view (FoV) where no active Ca^{2+} transients were visible. The same FoV cropping parameters were used throughout recordings from the same mice. Movies were then bandpassed with a spatial filter (low cutoff=0.005, high cutoff=0.500, Inscopix IDPS) and motion corrected (aligned to mean image or first frame, max_translation=20, Inscopix IDPS). Ca^{2+} traces were extracted with an adapted version of *CNMFe* (54) from Inscopix (see software table) with the following parameters (Cell diameter: 10 px, PNR: 10 for excitatory cells and 20 for GABAergic cells, Corr: 0.8). Ca^{2+} traces were manually curated with predefined selection criteria (peak amplitude >80 A.U., baseline drifts less than 20% of peak fluorescence, clear cell shape, locate outside blood vessels, minimal motion artifacts of given regions of interest).

Image stacks from 3P imaging were loaded into Suite2P (55) for motion correction, region-of-interest (ROI) segmentation and trace extraction using the settings specified in the appended exemplary .ops file. We used the 'mean img', 'correlation map', and 'max projection' views of Suite2P to manually check and sort somatic from non-somatic ROIs of mitral cells. The output from Suite2P was analyzed in Python: Detected neuropil signals were subtracted. Remaining frames with movement artifacts were then detected and excluded based on the presence of post-registration x- and y-shifts at each time point. A further criterion was the phase correlation of individual frames and the reference image below a threshold of 50% of the maximum peak of phase correlation in the respective stack. After that, $\Delta F/F$ values and z-scores were calculated in customized Python scripts.

Data analysis, statistics and plotting

All data analysis was performed using customized scripts in Python and R. Statistical analysis was performed in Python (Scipy, Numpy, Dabest) and R (Lmer). Individual statistical tests are listed under the respective figure legends and all statistical details are listed in the statistical summary table. Most figures were plotted in Python (matplotlib, seaborn) and figure and font sizes were later modified in Illustrator (Adobe). We used the Okabe-Ito color palette (56) to increase the accessibility of common forms of color blindness.

Data synchronization

Ca^{2+} imaging data and behavioral data were synchronized by finding the time lag of maximum cross-correlation between pump events in digital values from the PhenoSys behavioral protocol and the binarized pump-triggered TTL pulses recorded in the Inscopix system by Pynapple.cross_correlogram (Python).

Binge feeding bout detection and slow feeding processing

To detect binge feeding bouts, inter-pump intervals were calculated for each pump event, and only pump deliveries with intervals shorter than 2 s qualified as part of a feeding bout. Additionally, each feeding bout was required to include at least 3 pump deliveries.

Pump events in slow feeding mode were filtered out if no further lick event followed the initial lick event triggering pump activation. Initial motor artifacts from the movement of the lick spout were also removed from the further analysis. Since binge feeding bouts were guaranteed to have subsequent lick events by design, the exclusion of pump events following no lick events was not applied to binge feeding pump events.

Area Under the Receiver Operating Characteristics (auROC)

We used auROC to classify neurons into different response classes to Ensure and water deliveries during slow feeding (57; 58). In individual neurons, we compared the distribution of raw Ca^{2+} amplitudes during baseline activity (-1 to 0 s before pump activation) to the distribution of raw Ca^{2+} amplitudes in individual 100-ms bins across trials. To produce the bin-specific ROC curves, we moved a criterion from the minimal to the maximal Ca^{2+} response we found in the neuron's baseline activity distribution and the given 100 ms bin distribution. We then plotted the probability that Ca^{2+} signals in the given 100ms bin distribution were larger than the criterion against the probability that the Ca^{2+} signals in the baseline distribution were larger than the criterion. The auROC for each bin was then calculated using the auc function (sklearn.metrics.auc), resulting in auROC values between 0-1 and 0.5 means not different from the baseline. The post-stimulus auROC values from each time bin were compared to the baseline auROC values. Significance was established if at least four consecutive post-stimulus bin values between 0-2 s were greater than 2 S.D. of the pre-stimulus baseline values (food- or water-activated neurons).

Effect size calculation

To calculate the effect size of binge feeding-induced suppression in each neuron class, we performed a bootstrap-coupled estimation (DABEST, Python). To obtain the distribution of the mean difference between the two conditions, we re-sampled the mean Ca^{2+} activity of two conditions (eg. slow feeding and binge feeding) 5000 times (bootstrapping distribution, represented as the violin plot in Fig. 2e, 3m, and Fig S8a). The distribution was then normalized by the pooled standard derivation of both conditions to convert it to Cohen's d using the Dabest.cohens_d (DABEST). P values were computed with the Dabest.PermutationTest (DABEST).

Q values calculation

To estimate the differences between 2 neuronal time series along the time axis, we first calculated the P values of each time bin by performing the unpaired Student's t-test (scipy.stats.ttest_ind) and then applied false discovery rate correction (statsmodels.stats.multitest.fdrcorrection) to obtain the adjusted P values, which are the Q values.

Linear Mixed Models

Linear mixed models were used to estimate contributions of predictors (eg. level of excitation/suppression in neuronal activities upon feeding, or interaction of optogenetic actuators and light stimulation) to outcome (eg. food consumption or feeding bout duration) while allowing different intercepts for individual mice (lmer, R). To calculate the contribution of a given predictor, we built a full model with all predictors and a reduced model that lacks the given predictor. We then compared these two models with anova function (R) to calculate the P value of the given predictor. Representative models are structured as following:

Full model

$$Food.consumption \sim 1 + session.number + bodyweight + sex+ \\ virus.type + LED.state + virus.type * LED.state + (1|mouse.id)$$

Reduced model

$$Food.consumption \sim 1 + session.number + bodyweight + sex+ \\ virus.type + LED.state + (1|mouse.id)$$

Statistical analysis

Mean $\pm$ standard error of the mean (s.e.m.) or 95% confidence of interval were used to report statistics in figures. Applied statistical tests and the sample size for each analysis are listed in the figure legends and the statistical summary table. A significance level of p <0.05 is used for rejecting null hypothesis testing. No statistical methods were used to predetermine sample size randomization nor blinding was applied. All statistical analyses were performed in Python and R.

Histology and imaging

Mice were anesthetized with (100 mg/Kg) Ketamine and (15 mg/Kg) Xylazine and perfused with 0.1M PBS and then 4% paraformaldehyde (PFA). Mice brains were harvested and stored in 4% PFA at 4°C overnight and transferred to 0.1M PBS for long-term storage. Brains were embedded in 4% agar-agar and sliced at 100-150 μm thickness with a vibratome. Brain slices were mounted on glass slides and were imaged by an epifluorescence microscope (Leica DMi8) or a confocal microscope (Leica SP5). Acquired images were then aligned to the mouse brain atlas (59) for registration of the location of GRIN lens-prism or fiber optic cannula implants.

Serial 2-Photon tomography (Brainsaw)

A subset of fixed mice brains was sliced and imaged by serial 2P tomography, where whole forebrain structures can be imaged at cellular resolutions (60). We modified a custom-made 2P microscope (COSYS, UK) to operate with BakingTray (ScanImage & BakingTray, MATLAB). Obtained images were stitched (StitchIt, MATLAB) and reconstructed into 3D brain models. Image stacks were then registered to the Allen mouse brain atlas (BrainReg, Python) and visualized with napari (Python).

Tables of materials

Virus and construct

Table 2: Virus and construct table

Reagent or resource	**Source**	**Identifier (RRID)**
AAV1 pAAV.Syn.Flex.GCaMP6f.WPRE.SV40	Virus: Addgene	100833-AAV1 RRID:Addgene_100833
AAV8 pAAV-Syn-iCre-RFP	Plasmid: Charité viral core Virus: Charité viral core	Charité viral core id: BA-48c
AAV1 pGP-AAV-syn-jGCaMP7s-WPRE	Virus: Addgene	104487-AAV1 RRID:Addgene_104487
AAV9 pAAV-hSyn-Flex-OPN3-mScarlet-minWPRE	Plasmid: Charité viral core Virus: Charité viral core	Charité viral core id: BA-575b
AAV9 hSyn-flox-tdTomato	Plasmid: Charité viral core Virus: Charité viral core	Charité viral core id: BA-234a

Mouse line

Table 3: Mouse line table

Reagent or resource	**Source**	**Identifier (RRID)**
C57BL/6N	Charité Central Animal Facility	N/A
Ai93(TITL-GCaMP6f)-D	JAX	RRID:IMSR_JAX:024103
Rosa-tTA	JAX	RRID:IMSR_JAX:011008
Ai148(TIT2L-GC6f-ICL-tTA2)-D	JAX	RRID:IMSR_JAX:030328
CaMKII-CreT29	JAX	RRID:IMSR_JAX:005359
PV-Cre	JAX	RRID:IMSR_JAX:008069
SST-Cre	JAX	RRID:IMSR_JAX:013044

574 **Software**

Table 4: Software table

Reagent or resource	Source	Identifier (RRID/Version/reference)
FIJI/ ImageJ		RRID:SCR_002285 Version: 2.14.0/1.54f (61)
Python	Python Software Foundation	RRID:SCR_008394 Version: 3.9 (62)
Numpy		NumPy, RRID:SCR_008633 Version: 1.21.5 (63)
Matplotlib		MatPlotLib, RRID:SCR_008624 Version: 3.5.1 (64)
Seaborn		seaborn, RRID:SCR_018132 0.12.2 (65)
Scikit-learn		scikit-learn, RRID:SCR_002577 Version: 1.1.1 (66)
Statsmodels		statsmodel, RRID:SCR_016074 Version: 0.13.5 (67)
Scipy		SciPy, RRID:SCR_008058 Version: 1.8.0 (68)
Dabest		Version: 0.3.1 (69)
CNMFe/ CaImAn		Calcium Imaging data Analysis (54; 70), RRID:SCR_021533 Git forked version: https://github.com/flatironinstitute/CaImAn.git@ 7dc5b42ab06c6a6b86ff1520dfc5b2334f335a78
Inscopix *CNMFe* wrapper		https://github.com/inscopix/isx-cnmfe-wrapper@v1.2
Inscopix *CNMFe*	Inscopix	https://github.com/inscopix/inscopix-cnmfe
Inscopix python API	Inscopix	
Inscopix Data Processing Software	Inscopix	Version: 1.31, 1.6.0, 1.8.0
Bonsai		Bonsai, RRID:SCR_021512 (71)
Pyanpple		Version: 0.3.1 (72)

LSMAQ		https://github.com/danionella/lsmaq
Suite2P		https://github.com/MouseLand/suite2p RRID:SCR_016434 (55)
StichIt		https://github.com/SainsburyWellcomeCentre/StitchIt
BrainReg		https://github.com/brainglobe/brainreg (73)
Cellfinder		https://github.com/brainglobe/cellfinder (74)
BackingTray		https://github.com/SainsburyWellcomeCentre/BakingTray
R		Version: 4.2.2 RRID:SCR_001905 (75)
Rstudio		Version: 2022.12.0+353 RRID:SCR_000432 (76)
lme4		Version: 1.1.31 RRID:SCR_015654 (77)
Illustrator	Adobe	Version: 27.4.1, 2023 RRID:SCR_010279

Supplementary figures

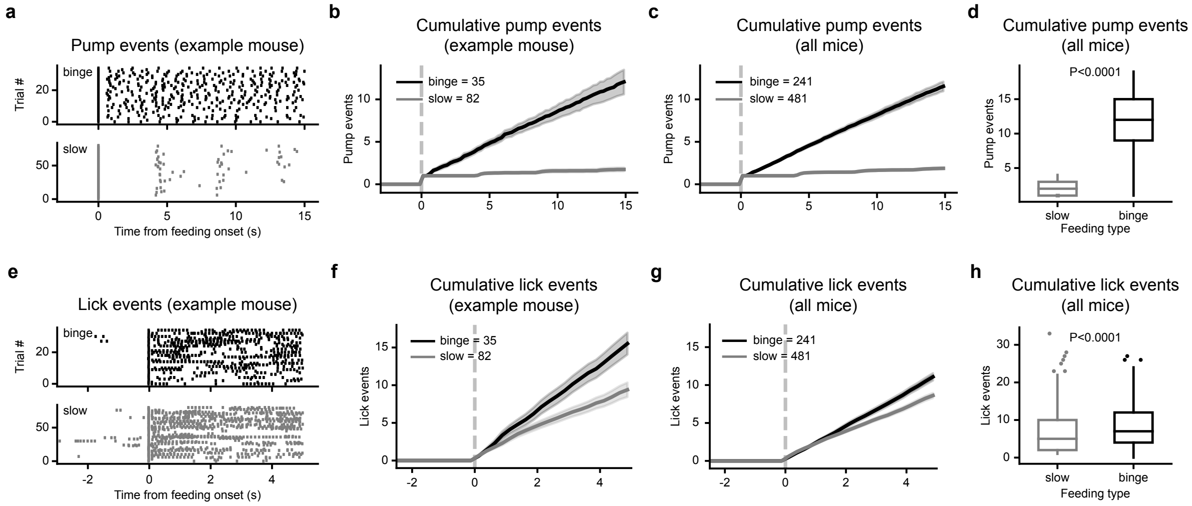

Figure. S1: **Behavioral differences between slow feeding and binge feeding.**
a, Pump delivery events for slow feeding and binge feeding from an example mouse. **b**, Cumulative pump events for slow feeding and binge feeding from an example mouse (same data as in **a**). **c**, Same as in **b**, but for all aPC CaMK2$^+$ mice (n= 481 for slow feeding trials and 241 trials for binge feeding trials from 8 mice). **d**, Quantification of cumulative pump events within 15 s after feeding bout onset. Unpaired Student's t-test (n is the same as in **c**). **e**, Lick events for slow feeding and binge feeding from an example mouse. **f**, Cumulative lick events for slow feeding and binge feeding from an example mouse (same data as in **e**). **g**, Same as in **f**, but for all aPC CaMK2$^+$ mice (n is the same as in **c**). **h**, Quantification of cumulative lick events in 4 s after the onset of feeding bouts. Unpaired Student's t-test (n is the same as in **c**)

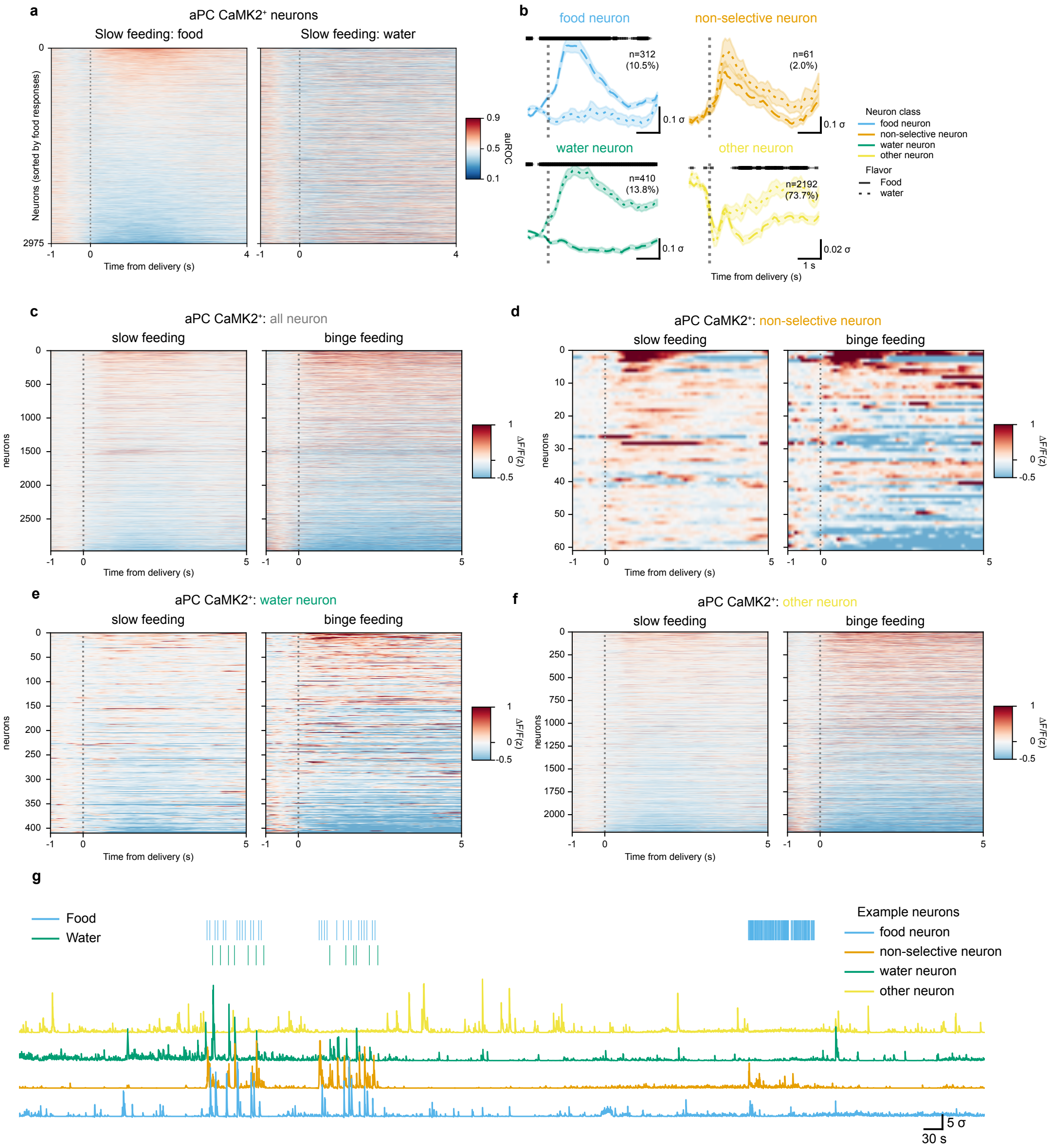

Figure. S2: **aPC CaMK2$^+$ neuronal responses upon slow feeding and binge feeding.**
a, Area Under the Receiver Operating Characteristics (auROC) curve of aPC CaMK2$^+$ neurons during slow feeding (see **Methods**, n is 2975 cells from 8 mice). **b**, Slow feeding responses of aPC CaMK2$^+$ neuronal subclasses for food and water deliveries (n=312 food neurons, 61 non-selective neurons, 410 water neurons, 2192 other neurons from 8 mice). The shaded line above denotes the adjusted P-values (Q-values) of each time point, with different line widths representing different values (from thin to thick: q <0.05, <0.01, <0.001). **c**, Responses of individual aPC CaMK2$^+$ neurons upon slow feeding and binge feeding (n is the same as in **a**). **d**, Same as in **c**, but with non-selective consumption neurons (n=61 cells from 8 mice). **e**, Same as in **c**, but with water-activated neurons (n=410 cells from 8 mice). **f**, Same as in **c**, but with non-responding neurons (n=2192 cells from 8 mice). **g**, Example traces of aPC CaMK2$^+$ neurons from a recording session.
For **b**, data are shown as mean ± s.e.m.

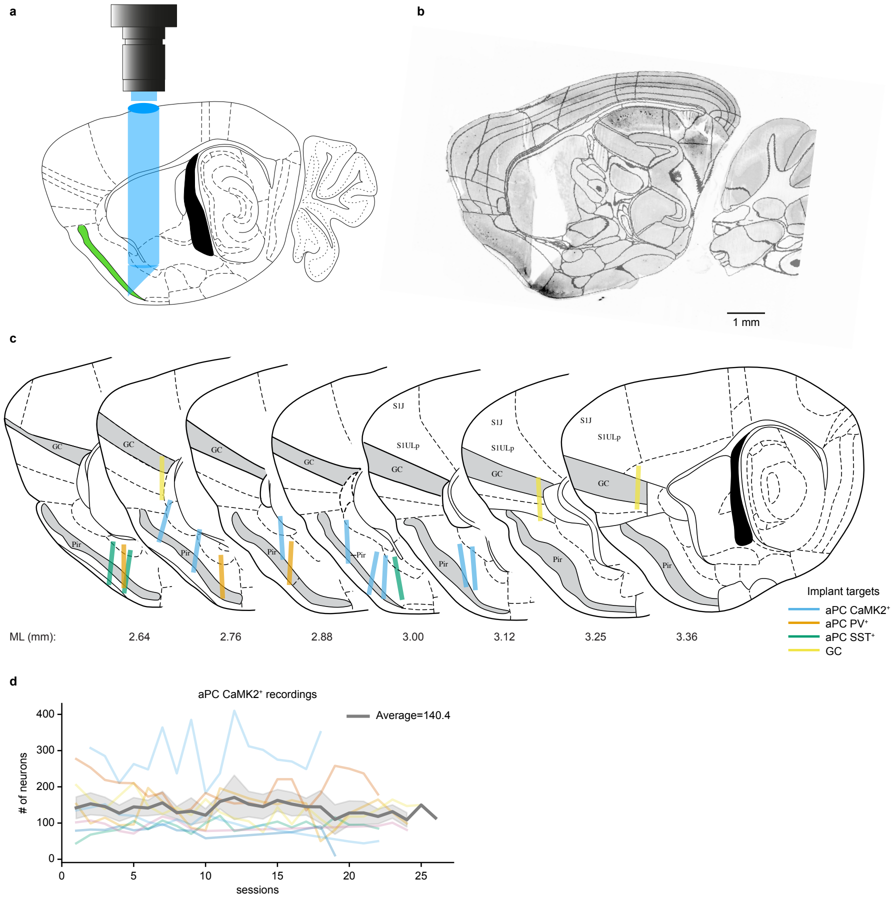

Figure. S3: **GRIN lens-Prism Implant coordinates and extracted cell numbers throughout experimental sessions.**

a, Schematic of implant coordination in the aPC. **b**, GRIN lens-Prism path and GCaMP6f expression from an example mouse. **c**, Reconstructed GRIN len-Prism coordinates in different cell types in the aPC (Fig.1, Fig.3) and GC (Fig.2). **d**, Numbers of aPC CaMK2$^+$ neurons extracted with *CNMFe* on each recording session (n= 8 mice).

For **d**, data are shown as mean ± s.e.m.

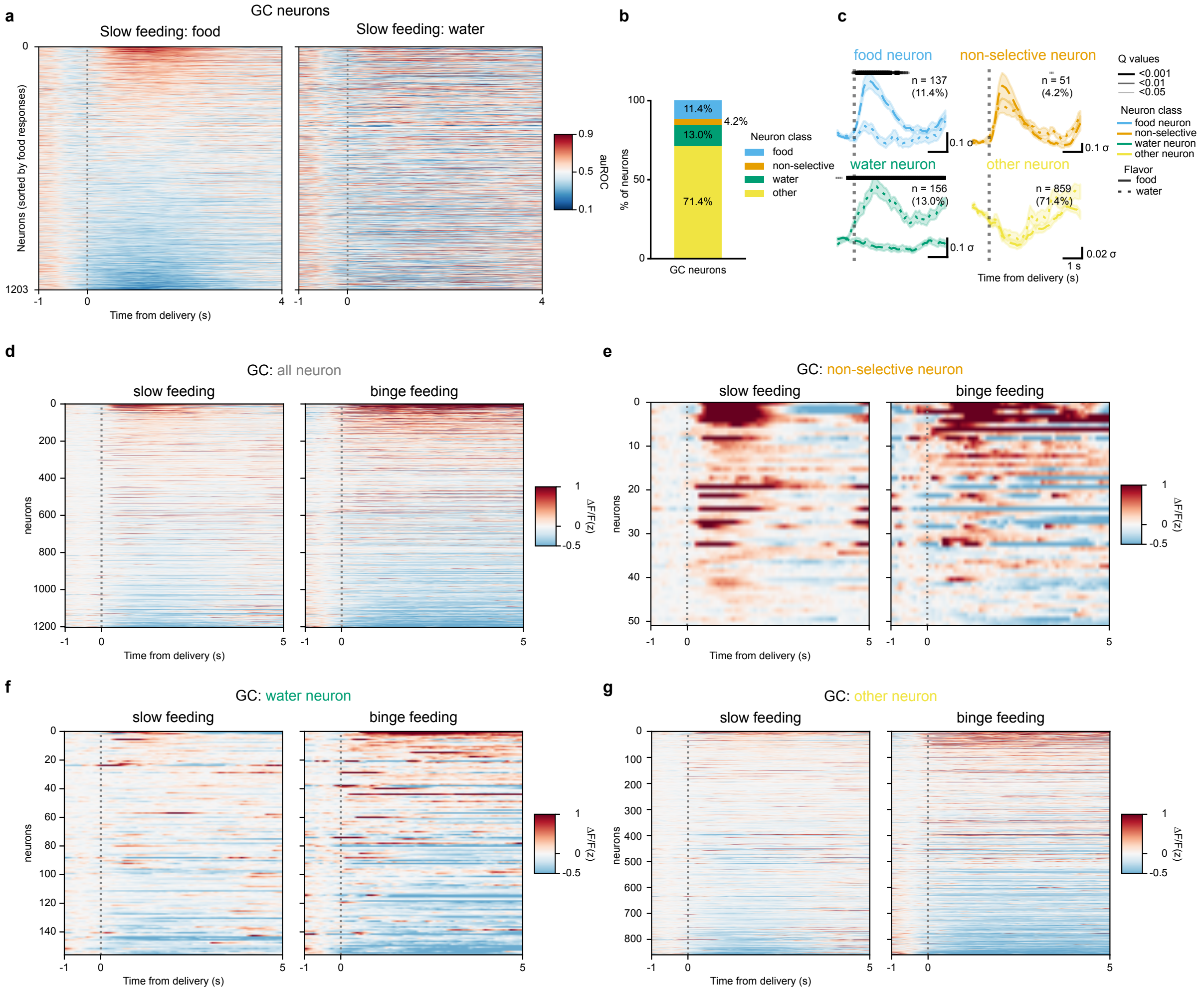

Figure. S4: **GC neuronal responses upon slow feeding and binge feeding.**
a, Area Under the Receiver Operating Characteristics (auROC) curve of GC neurons during slow feeding (see **Methods**). **b**, Proportion of GC subclasses (n=1203 all neurons, 137 food neurons, 51 non-selective neurons, 156 water neurons, and 859 other neurons from 3 mice). **c**, Food responses of subclasses of GC neurons during slow feeding for food and water deliveries (n is the same as in **b**). The shaded line above denotes the adjusted P-values (Q-values) of each time point, with different line widths representing different values (from thin to thick: q <0.05, <0.01, <0.001). **d**, Responses of all GC neurons upon slow feeding and binge feeding (n=1203 cells from 3 mice). **e**, Same as in **d**, but with non-selective consumption neurons (n=51 cells from 3 mice). **f**, Same as in **d**, but with water-activated neurons (n=156 cells from 3 mice). **g**, Same as in **d**, but with non-responding neurons (n=859 cells from 3 mice).
For **c**, data are shown as mean ± s.e.m.

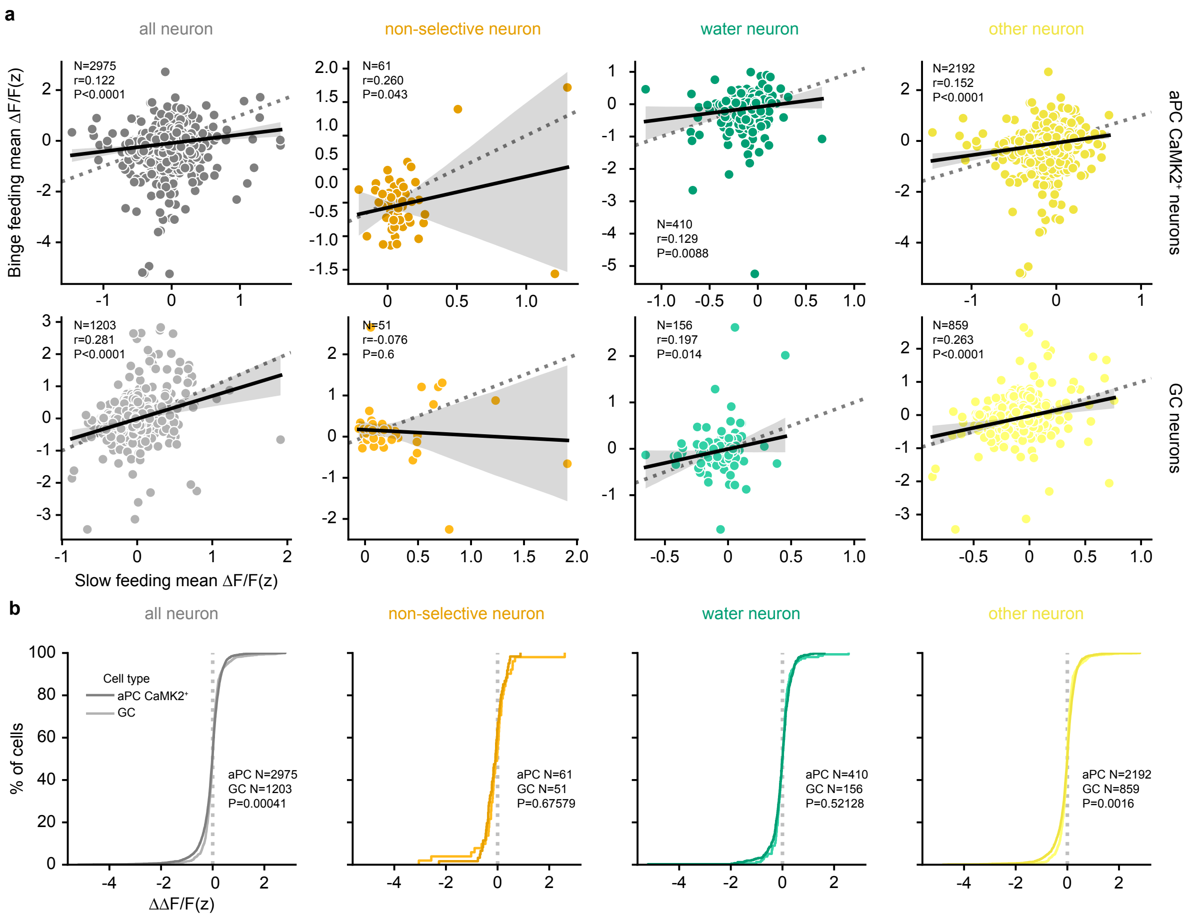

Figure. S5: **Distinct binge feeding-induced modulation in the aPC and the GC.**
a, Cell-wise comparison of neuronal responses upon slow feeding and binge feeding (For aPC CaMK2$^+$ neurons, n=2975 for all neurons, 61 for non-selective neurons, 410 for water neurons, 2192 for other neurons from 8 mice. For GC neurons, n=1203 for all neurons, 51 for non-selective neurons, 156 for water neurons, and 859 for other neurons from 3 mice). **b**, Cumulative distribution of the difference for each cell upon slow and binge feeding (binge feeding - slow feeding, ΔΔ F/F(z), n is the same as in **a**) In **a**, r and P represent the correlation coefficient and P-value of Pearson's r.

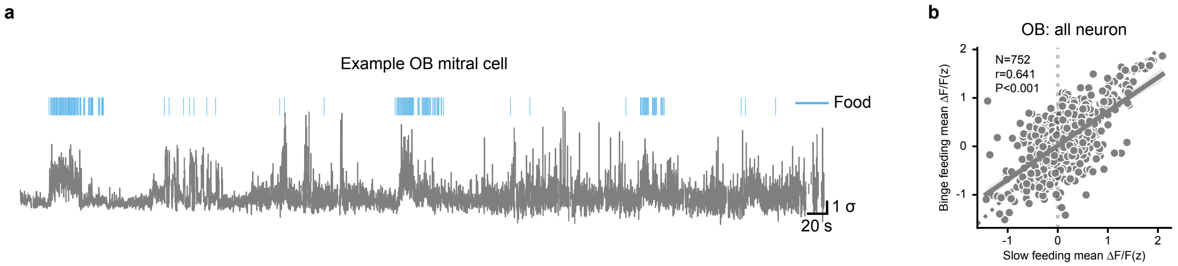

Figure. S6: **OB mitral cell example trace and cell-wise comparison.**
a, An example trace from an OB mitral cell upon slow feeding and binge feeding. **b**, Cell-wise comparison of neuronal responses upon slow feeding and binge feeding (n=752 cells from 4 mice).
In **b**, r and P represent the correlation coefficient and P-value of Pearson's r.

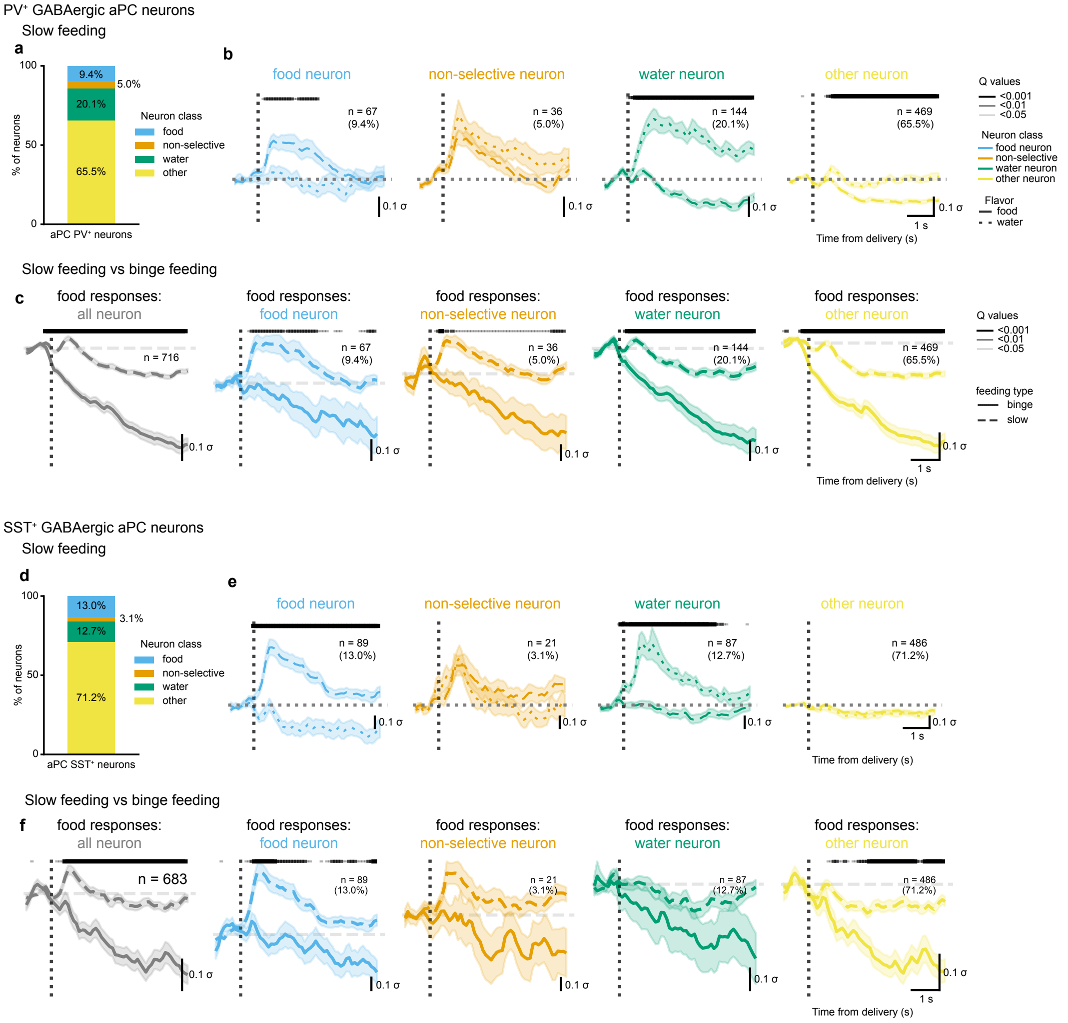

Figure. S7: **aPC GABAergic neuronal responses to slow feeding and binge feeding.**

a, Proportion of aPC PV$^+$ subclasses (n=67 cells for food neurons, 36 cells for non-selective neurons, 144 cells for water neurons, 469 cells for other neurons from 3 mice). **b**, Responses of subclasses of aPC PV$^+$ neurons during slow feeding for food and water deliveries (n is the same as in **a**, except n= 716 cells for all neurons). **c**, Food responses aPC PV$^+$ neuron subclasses during slow feeding and binge feeding (n is the same as in **b**). **d**, Same as in **a**, but for aPC SST$^+$neurons (n=89 cells for food neurons, 21 cells for non-selective neurons, 87 cells for water neurons, 486 cells for other neurons from 3 mice). **e**, Same as in **b**, but for aPC SST$^+$neurons (n is the same as in **d**). **f**, Same as in **c**, but for aPC SST$^+$neurons (n is the same as in **e**, except n=683 cells in all neurons). The shaded line above denotes the adjusted P-values (Q-values) of each time point, with different line widths representing different values (from thin to thick: Q <0.05, <0.01, <0.001).

For **b**,**c**,**e**,**f**, data are shown as mean ± s.e.m.

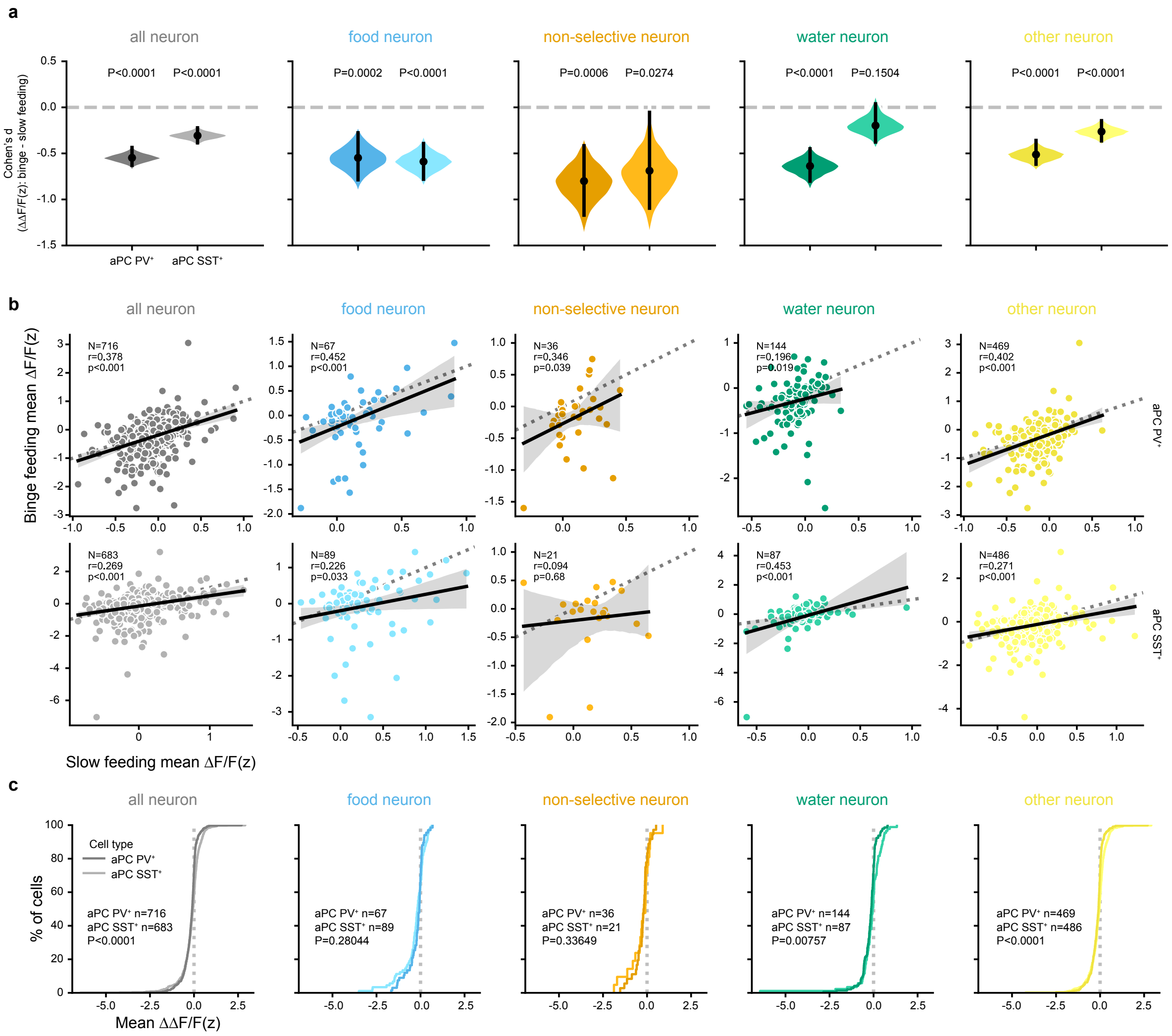

Figure. S8: **Cell-wise comparison of aPC GABAergic neuronal responses to slow feeding and binge feeding.**

a, Estimated effect size of binge feeding-induced suppression in aPC PV^+ and aPC SST^+ subclasses (For aPC PV^+ neurons, n=716 cells for all neurons, 67 cells for food neurons, 36 cells for non-selective neurons, 144 cells for water neurons, 469 cells for other neurons from 3 mice. For aPC SST^+ neurons, n=683 cells for all neurons, n=89 cells for food neurons, 21 cells for non-selective neurons, 87 cells for water neurons, 486 cells for other neurons from 3 mice). **b**, Cell-wise comparison of neuronal responses upon slow feeding and binge feeding in aPC PV^+ and aPC SST^+ subclasses (n is the same as in **a**). **c**, Cumulative distribution of the difference for each cell upon slow and binge feeding (binge feeding - slow feeding, ΔΔ F/F(z)) in aPC PV^+ and aPC SST^+ subclasses (n is the same as in **a**).

For **b**, r and P represent the correlation coefficient and P-value of Pearson's r.

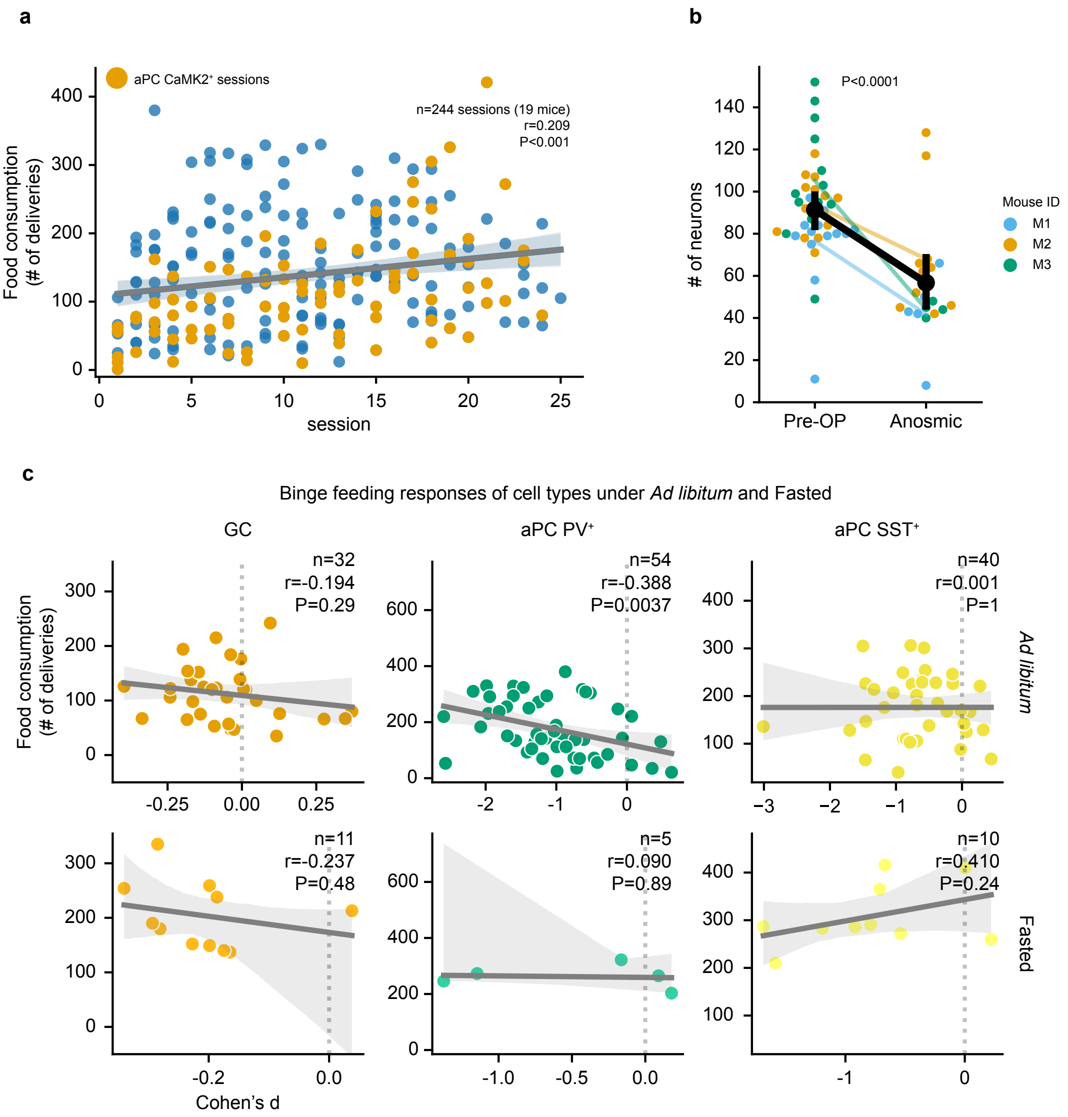

Figure. S9: **Effects of temporal progression, anosmia, and fasting.**

a, Food consumption (number of food deliveries) on subsequent recording sessions (n=244 sessions from 19 mice). Orange dots are mice with recordings in aPC CaMK2$^+$ cells (n=84 sessions from 8 mice), blue dots represent all other mice. **b**, Number of extracted cells in aPC CaMK2$^+$ mice before and after Triton-X100 application (n=21 Pre-OP sessions and 15 anosmic sessions from the same 3 mice). Colors represent recordings from each mouse. **c**, Neuronal responses to binge feeding in the GC, aPC PV$^+$, and aPC SST$^+$ under *ad libitum* (upper row) and fasting (lower row) conditions plotted against consumption (For GC, n=32 *ad libitum* sessions and 11 fasted sessions from 3 mice. For aPC PV$^+$, n=54 *ad libitum* sessions and 11 fasted sessions from 3 mice. For aPC SST$^+$, n=40 *ad libitum* sessions and 10 fasted sessions from 3 mice.).

For **b**, data are shown as mean ± s.e.m. For **a**,**c**, r and P represent the correlation coefficient and P-value of Pearson's r.

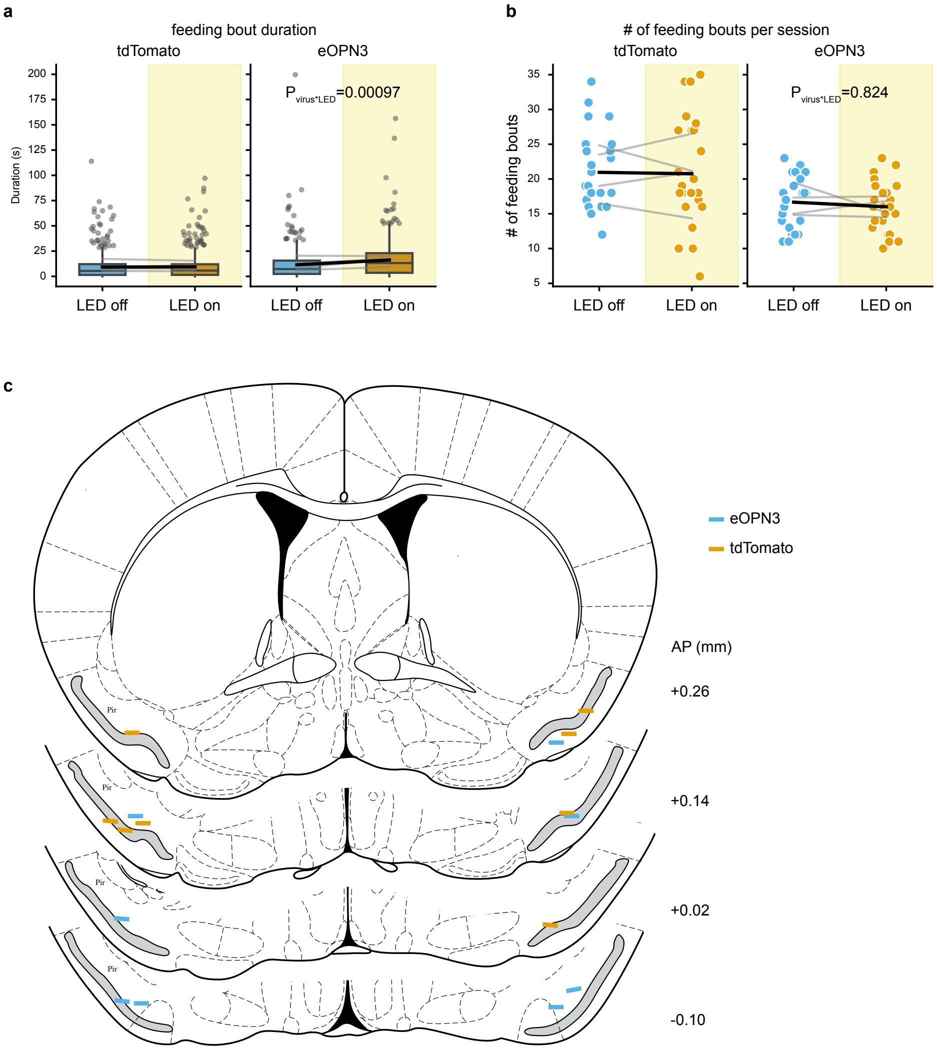

Figure. S10: **Effects of optogenetic suppression of aPC and implant coordinates.**
a, Effects of light stimulation on the duration of individual feeding bouts in tdTomato- and eOPN3-expressing mice (n=569 feeding bouts in LED off sessions and 562 feeding bouts in LED on sessions from 4 tdTomato mice. n=431 feeding bouts in LED off sessions and 425 feeding bouts in LED on sessions from 4 eOPN3 mice). **b**, Effects of light stimulation on the number of feeding bouts per experimental session in tdTomato- and eOPN3-expressing mice (n=24 LED off sessions and 24 LED on sessions from 4 tdTomato mice and n=24 LED off sessions and 24 LED on sessions from 4 eOPN3 mice). Grey lines denote the data from the same mice, and the black line denotes the overall mean of the data. The p values are calculated from a linear mixed model. **c**, Implant coordinates of optical fibers.
For the box plot in a and b, the center line shows the median, the box limits show the quartiles, the whiskers show 1.5x the interquartile range, and the points show the outliers.

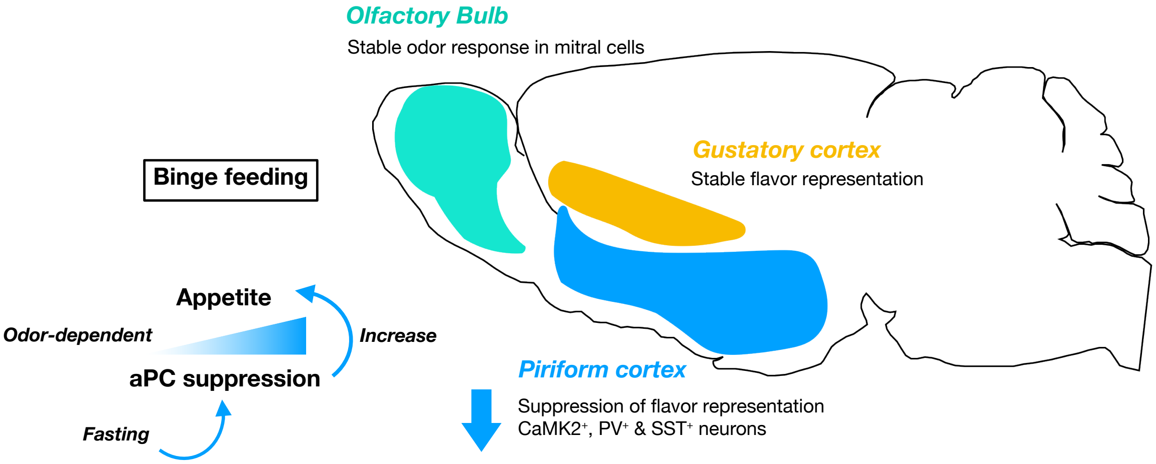

Figure. S11: **Graphic summary.**
In this study, we found a feeding rate-dependent suppression of the olfactory flavor representation (Fig. 1 and Fig. 3) whereas the gustatory flavor representation is not affected by the feeding rate (Fig. 2). Olfactory inputs from the olfactory bulb remain stable across feeding rates (Fig. 3). We found the magnitude of binge feeding-induced aPC suppression correlates with appetite and the correlation depends on olfactory perception and metabolic state (Fig. 4). We further showed optogenetically suppression in the aPC upon feeding promotes appetite (Fig. 5).

Supplementary Videos

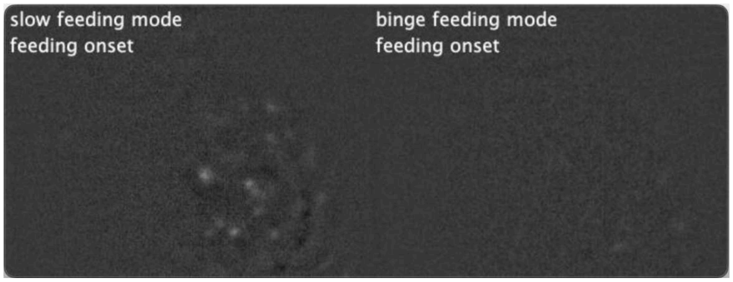

Video. S1: **Example Ca^{2+} video during slow feeding and binge feeding.**
Left panel: Ca^{2+} transients of aPC CaMK2^{+} neurons during slow feeding. Right panel: Ca^{2+} transients of aPC CaMK2^{+} neurons during binge feeding from the same recording, the same mice.

References

[1] Scisco, J. L., Muth, E. R., Dong, Y. & Hoover, A. W. Slowing bite-rate reduces energy intake: an application of the bite counter device. *J. Am. Diet. Assoc.* **111**, 1231–1235 (2011).

[2] Andrade, A. M., Greene, G. W. & Melanson, K. J. Eating slowly led to decreases in energy intake within meals in healthy women. *J. Am. Diet. Assoc.* **108**, 1186–1191 (2008).

[3] Bolhuis, D. P., Lakemond, C. M. M., de Wijk, R. A., Luning, P. A. & de Graaf, C. Consumption with large sip sizes increases food intake and leads to underestimation of the amount consumed. *PLoS One* **8**, e53288 (2013).

[4] Teo, P. S., van Dam, R. M. & Forde, C. G. Combined impact of a faster Self-Reported eating rate and higher dietary energy intake rate on energy intake and adiposity. *Nutrients* **12** (2020).

[5] Hurst, Y. & Fukuda, H. Effects of changes in eating speed on obesity in patients with diabetes: a secondary analysis of longitudinal health check-up data. *BMJ Open* **8**, e019589 (2018).

[6] Bolhuis, D. P., Lakemond, C. M. M., de Wijk, R. A., Luning, P. A. & de Graaf, C. Both a higher number of sips and a longer oral transit time reduce ad libitum intake. *Food Qual. Prefer.* **32**, 234–240 (2014).

[7] Mattes, R. Soup and satiety. *Physiol. Behav.* **83**, 739–747 (2005).

[8] Slyper, A. Oral processing, satiation and obesity: Overview and hypotheses. *Diabetes Metab. Syndr. Obes.* **14**, 3399–3415 (2021).

[9] Samakidou, G. E., Koliaki, C. C., Liberopoulos, E. N. & Katsilambros, N. L. Non-Classical aspects of obesity pathogenesis and their relative clinical importance for obesity treatment. *Healthcare (Basel)* **11** (2023).

[10] Grove, J. C. R. *et al.* Dopamine subsystems that track internal states. *Nature* **608**, 374–380 (2022).

[11] Chen, Y., Lin, Y.-C., Kuo, T.-W. & Knight, Z. A. Sensory detection of food rapidly modulates arcuate feeding circuits. *Cell* **160**, 829–841 (2015).

[12] Mandelblat-Cerf, Y. *et al.* Arcuate hypothalamic AgRP and putative POMC neurons show opposite changes in spiking across multiple timescales. *Elife* **4** (2015).

[13] Cecil, J. E., Francis, J. & Read, N. W. Comparison of the effects of a high-fat and high-carbohydrate soup delivered orally and intragastrically on gastric emptying, appetite, and eating behaviour. *Physiol. Behav.* **67**, 299–306 (1999).

[14] Betley, J. N. *et al.* Neurons for hunger and thirst transmit a negative-valence teaching signal. *Nature* **521**, 180–185 (2015).

[15] Buzsáki, G. *The Brain from Inside Out*, vol. 51 (Oxford University Press, 2019).

[16] Small, D. M. Flavor is in the brain. *Physiol. Behav.* **107**, 540–552 (2012).

[17] Elliott, V. E. & Maier, J. X. Multisensory interactions underlying flavor consumption in rats: the role of experience and unisensory component liking. *Chem. Senses* **45**, 27–35 (2020).

[18] Blazing, R. M. & Franks, K. M. Odor coding in piriform cortex: mechanistic insights into distributed coding (2020).

[19] Choi, G. B. *et al.* Driving opposing behaviors with ensembles of piriform neurons. *Cell* **146**, 1004–1015 (2011).

[20] Wang, P. Y. *et al.* Transient and persistent representations of odor value in prefrontal cortex. *Neuron* **108**, 209–224.e6 (2020).

[21] Miura, K., Mainen, Z. F. & Uchida, N. Odor representations in olfactory cortex: distributed rate coding and decorrelated population activity. *Neuron* **74**, 1087–1098 (2012).

[22] Stettler, D. D. & Axel, R. Representations of odor in the piriform cortex. *Neuron* **64**, 292 (2009).

[23] Wilson, D. A. & Sullivan, R. M. Cortical processing of odor objects. *Neuron* **72**, 506–519 (2011).

[24] Bolding, K. A. & Franks, K. M. Complementary codes for odor identity and intensity in olfactory cortex. *Elife* **6** (2017).

[25] Berners-Lee, A., Shtrahman, E., Grimaud, J. & Murthy, V. N. Experience-dependent evolution of odor mixture representations in piriform cortex. *PLoS Biol.* **21**, e3002086 (2023).

[26] Tantirigama, M. L. S., Huang, H. H.-Y. & Bekkers, J. M. Spontaneous activity in the piriform cortex extends the dynamic range of cortical odor coding. *Proc. Natl. Acad. Sci. U. S. A.* **114**, 2407–2412 (2017).

[27] Roland, B., Deneux, T., Franks, K. M., Bathellier, B. & Fleischmann, A. Odor identity coding by distributed ensembles of neurons in the mouse olfactory cortex. *Elife* **6**, 14255 (2017).

[28] Bimbard, C. *et al.* Behavioral origin of sound-evoked activity in mouse visual cortex. *Nat. Neurosci.* **26**, 251–258 (2023).

[29] Christensen, A. J. & Pillow, J. W. Reduced neural activity but improved coding in rodent higher-order visual cortex during locomotion. *Nat. Commun.* **13**, 1676 (2022).

[30] de Oliveira, E. F. *et al.* Off-manifold coding in visual cortex revealed by sleep (2022).

[31] Musall, S., Kaufman, M. T., Juavinett, A. L., Gluf, S. & Churchland, A. K. Single-trial neural dynamics are dominated by richly varied movements. *Nat. Neurosci.* **22**, 1677–1686 (2019).

[32] Steinmetz, N. A., Zatka-Haas, P., Carandini, M. & Harris, K. D. Distributed coding of choice, action and engagement across the mouse brain. *Nature* **576**, 266–273 (2019).

[33] Stringer, C. *et al.* Spontaneous behaviors drive multidimensional, brainwide activity. *Science* **364**, 255 (2019).

[34] Frank, T., Mönig, N. R., Satou, C., Higashijima, S.-I. & Friedrich, R. W. Associative conditioning remaps odor representations and modifies inhibition in a higher olfactory brain area. *Nat. Neurosci.* **22**, 1844–1856 (2019).

[35] Bekkers, J. M. & Suzuki, N. Neurons and circuits for odor processing in the piriform cortex. *Trends Neurosci.* **36**, 429–438 (2013).

[36] Poo, C. & Isaacson, J. S. A major role for intracortical circuits in the strength and tuning of odor-evoked excitation in olfactory cortex. *Neuron* **72**, 41–48 (2011).

[37] Bolding, K. A. & Franks, K. M. Recurrent cortical circuits implement concentration-invariant odor coding. *Science* **361**, 1088–+ (2018).

[38] Large, A. M., Vogler, N. W., Mielo, S. & Oswald, A.-M. M. Balanced feedforward inhibition and dominant recurrent inhibition in olfactory cortex. *Proc. Natl. Acad. Sci. U. S. A.* **113**, 2276–2281 (2016).

[39] Cummings, D. M., Emge, D. K., Small, S. L. & Margolis, F. L. Pattern of olfactory bulb innervation returns after recovery from reversible peripheral deafferentation. *J. Comp. Neurol.* **421**, 362–373 (2000).

[40] Soria-Gómez, E. *et al.* The endocannabinoid system controls food intake via olfactory processes. *Nat. Neurosci.* **17**, 407–415 (2014).

[41] Aimé, P. *et al.* Fasting increases and satiation decreases olfactory detection for a neutral odor in rats. *Behav. Brain Res.* **179**, 258–264 (2007).

[42] Freeman, W. J. Correlation of elctrical activity of prepyriform cortex and behavior in cat. *J. Neurophysiol.* **23**, 111–131 (1960).

[43] Prud'homme, M. J. *et al.* Nutritional status modulates behavioural and olfactory bulb fos responses to isoamyl acetate or food odour in rats: roles of orexins and leptin. *Neuroscience* **162**, 1287–1298 (2009).

[44] Albrecht, J. *et al.* Olfactory detection thresholds and pleasantness of a food-related and a non-food odour in hunger and satiety. *Rhinology* **47**, 160–165 (2009).

[45] Mahn, M. *et al.* Efficient optogenetic silencing of neurotransmitter release with a mosquito rhodopsin. *Neuron* **109**, 1621–1635.e8 (2021).

[46] Shepherd, G. M. Smell images and the flavour system in the human brain. *Nature* **444**, 316–321 (2006).

[47] Maier, J. X., Blankenship, M. L., Li, J. X. & Katz, D. B. A multisensory network for olfactory processing. *Curr. Biol.* **25**, 2642–2650 (2015).

[48] Riera, C. E. *et al.* The sense of smell impacts metabolic health and obesity. *Cell Metab.* **26**, 198–211.e5 (2017).

[49] Tucker, K., Overton, J. M. & Fadool, D. A. Diet-induced obesity resistance of kv1.3-/- mice is olfactory bulb dependent. *J. Neuroendocrinol.* **24**, 1087–1095 (2012).

[50] Berkun, M. M., Kessen, M. L. & Miller, N. E. Hunger-reducing effects of food by stomach fistula versus food by mouth measured by a consummatory response. *J. Comp. Physiol. Psychol.* **45**, 550–554 (1952).

[51] Stratton, R. J. & Elia, M. The effects of enteral tube feeding and parenteral nutrition on appetite sensations and food intake in health and disease. *Clin. Nutr.* **18**, 63–70 (1999).

[52] Hall, K. D. *et al.* Ultra-Processed diets cause excess calorie intake and weight gain: An inpatient randomized controlled trial of ad libitum food intake. *Cell Metab.* **30**, 67–77.e3 (2019).

[53] Ohkuma, T. *et al.* Association between eating rate and obesity: a systematic review and meta-analysis. *Int. J. Obes.* **39**, 1589–1596 (2015).

[54] Zhou, P. *et al.* Efficient and accurate extraction of in vivo calcium signals from microendoscopic video data. *Elife* **7**, 3237–3270 (2018).

[55] Pachitariu, M. *et al.* Suite2p: beyond 10,000 neurons with standard two-photon microscopy. Tech. Rep. (2016).

[56] Ichihara, Y. G. *et al.* Color universal design: the selection of four easily distinguishable colors for all color vision types. In Eschbach, R., Marcu, G. G. & Tominaga, S. (eds.) *Color Imaging XIII: Processing, Hardcopy, and Applications* (SPIE, 2008).

[57] Botta, P. *et al.* An amygdala circuit mediates Experience-Dependent momentary arrests during exploration. *Cell* **183**, 605–619.e22 (2020).

[58] Cohen, J. Y., Haesler, S., Vong, L., Lowell, B. B. & Uchida, N. Neuron-type-specific signals for reward and punishment in the ventral tegmental area. *Nature* **482**, 85–88 (2012).

[59] Paxinos, G. & Keith B. J. Franklin, M. *The Mouse Brain in Stereotaxic Coordinates* (Elsevier Science, 2007). URL https://books.google.de/books?id=5MdpQgAACAAJ.

[60] Ragan, T. *et al.* Serial two-photon tomography for automated ex vivo mouse brain imaging. *Nat. Methods* **9**, 255–258 (2012).

[61] Schindelin, J. *et al.* Fiji: an open-source platform for biological-image analysis. *Nat. Methods* **9**, 676–682 (2012).

[62] van Rossum, G. & de Boer, J. Interactively testing remote servers using the python programming language. *CWI Quarterly* **4**, 283–304 (1991).

[63] Harris, C. R. *et al.* Array programming with NumPy. *Nature* **585**, 357–362 (2020). URL https://doi.org/10.1038/s41586-020-2649-2.

[64] Hunter, J. D. Matplotlib: A 2d graphics environment. *Computing in Science & Engineering* **9**, 90–95 (2007).

[65] Waskom, M. L. seaborn: statistical data visualization. *Journal of Open Source Software* **6**, 3021 (2021). URL https://doi.org/10.21105/joss.03021.

[66] Pedregosa, F. *et al.* Scikit-learn: Machine learning in Python. *Journal of Machine Learning Research* **12**, 2825–2830 (2011).

[67] Seabold, S. & Perktold, J. statsmodels: Econometric and statistical modeling with python. In *9th Python in Science Conference* (2010).

[68] Virtanen, P. *et al.* SciPy 1.0: Fundamental Algorithms for Scientific Computing in Python. *Nature Methods* **17**, 261–272 (2020).

[69] Ho, J., Tumkaya, T., Aryal, S., Choi, H. & Claridge-Chang, A. Moving beyond P values: data analysis with estimation graphics. *Nat. Methods* **16**, 565–566 (2019).

[70] Giovannucci, A. *et al.* Caiman: An open source tool for scalable calcium imaging data analysis. *eLife* **8**, e38173 (2019).

[71] Lopes, G. *et al.* Bonsai: an event-based framework for processing and controlling data streams. *Front. Neuroinform.* **9**, 7 (2015).

[72] Viejo, G. *et al.* Pynapple, a toolbox for data analysis in neuroscience (2023).

[73] Claudi, F. *et al.* BrainGlobe atlas API: a common interface for neuroanatomical atlases. *J. Open Source Softw.* **5**, 2668 (2020).

[74] Tyson, A. L. *et al.* A deep learning algorithm for 3D cell detection in whole mouse brain image datasets. *PLoS Comput. Biol.* **17**, e1009074 (2021).

[75] R Core Team. *R: A Language and Environment for Statistical Computing*. R Foundation for Statistical Computing, Vienna, Austria (2021). URL https://www.R-project.org/.

[76] Posit team. *RStudio: Integrated Development Environment for R*. Posit Software, PBC, Boston, MA (2022). URL http://www.posit.co/.

[77] Bates, D., Mächler, M., Bolker, B. & Walker, S. Fitting linear mixed-effects models using lme4. *Journal of Statistical Software* **67**, 1–48 (2015).